Composite Structures 303 (2023) 116334

Contents lists available at ScienceDirect

Composite Structures

journal homepage: www.elsevier.com/locate/compstruct

Data-driven multi-objective optimization of ultralight hierarchical origami-corrugation *meta*-sandwich structures

Zengshen Yue [a,b,c], Bin Han [b,*], Zeyu Wang [b], Mao Yang [a], Qi Zhang [b], Tian Jian Lu [c,d,*]

[a] State Key Laboratory for Strength and Vibration of Mechanical Structures, Xi'an Jiaotong University, Xi'an 710049, PR China
[b] School of Mechanical Engineering, Xi'an Jiaotong University, Xi'an 710049, PR China
[c] Nanjing Center for Multifunctional Lightweight Materials and Structures (MLMS), Nanjing University of Aeronautics and Astronautics, Nanjing 210016, PR China
[d] State Key Laboratory of Mechanics and Control of Mechanical Structures, Nanjing University of Aeronautics and Astronautics, Nanjing 210016, PR China

ARTICLE INFO

Keywords:
Origami-corrugation *meta*-sandwich
Compressive performance
Fully connected neural networks
Optimal design

ABSTRACT

With advantages in stiffness, strength, and energy absorption, hierarchical origami-corrugation *meta*-sandwich (HOCM) structures are envisioned as a novel ultralight multifunctional sandwich construction for various practical applications. Firstly, the macro-equivalent compressive modulus is analytically derived using a two-level homogenization approach. The HOCM samples manufactured by selective laser melting are then tested under quasi-static out-of-plane compressive loading. A representative volume element model is proposed for finite element simulations to explore further the compressive performance, with good agreement achieved between measurements and simulations. Influences of critical geometric parameters on compressive properties, including initial failure modes, specific peak strength (SPS) and specific energy absorption (SEA), are numerically analyzed. Subsequently, the surrogate model based on a fully connected neural network algorithm is selected as the machine learning strategy to approximate the SPS and SEA, with cross-validation conducted to verify its accuracy. Finally, a multi-objective optimization method incorporating the surrogate model and the non-dominated sorting genetic algorithm II is implemented to carry out optimal design for HOCM structures possessing simultaneous superior SPS, SEA with assured stiffness. Such a data-driven optimization procedure based on the machine learning method exhibits high accuracy for strongly nonlinear problems, especially for SEA in current work, leading to highly efficient optimization.

1. Introduction

An excellent lesson learned from nature is that evolving cellular structures could become highly mechanically efficient at ultralight-weight, such as honeycomb-like structures (e.g., wood and cork [1]) and foam-like structures (e.g., plant parenchyma [2] and trabecular bone [3]). For example, the hornbill beak can be described as a sandwich-structured composite with a lightweight cellular core, which possesses a high stiffness-to-weight ratio and good shock resistance [4]. Inspired by these natural structures, diverse cellular mechanical metamaterials were proposed and investigated in recent years, which define their mechanical performance by geometry rather than composition [5,6]. Typically, rationally designed artificial mechanical metamaterials enable mechanical properties inaccessible with ordinary materials, such as twists under axial loading [7], negative Poisson ratio [8], hyper-elasticity [9], superior in-plane deformations [10,11], and so forth. Among the mechanical metamaterials, the origami structures attracted increasing attention [12]. Compared to traditional cellular structures such as corrugations and honeycombs, origami structures exhibit the combined property of improved structural stability and fluid-through feature [13]. Nevertheless, their energy absorption capacity is a bit weaker than that of honeycombs due to fewer plastic hinges formed under out-of-plane compression [13], thus requiring further improvement.

Due to composition-independence, a rational geometric design is essential for mechanical metamaterials. Hierarchy design has become popular for designing artificial structures with superior mechanical properties, such as polymers [14], composites [15–17], and *meta*-sandwich cores [18,19]. In particular, for *meta*-sandwich cores, the concept of hierarchical corrugated structure was proposed [18]; the resulting hierarchical corrugated core made from structural alloy possessed significantly higher collapse strengths compared to its equivalent mass

* Corresponding authors.
E-mail addresses: hanbinghost@mail.xjtu.edu.cn (B. Han), tjlu@nuaa.edu.cn (T.J. Lu).

https://doi.org/10.1016/j.compstruct.2022.116334
Received 18 April 2022; Received in revised form 3 August 2022; Accepted 7 October 2022
Available online 13 October 2022
0263-8223/© 2022 Elsevier Ltd. All rights reserved.

first-order counterpart. Further, both the in-plane quasi-static and dynamic crushing properties of a second-order hierarchical honeycomb metamaterial were studied [20], with its cell walls replaced by corrugation sandwich panels. Under quasi-static crushing, hierarchical honeycombs provided significant improvement in the collapse stress over first-order honeycombs; however, as the crushing velocity was gradually increased, the improvement decreased [20]. Besides, hierarchically architected lattice metamaterials with octahedron-of-octahedra and octet-of-octahedra topologies were manufactured from Ti-6Al-4V alloy sheets using a "snap-fit" assembly technique combined with vacuum brazing [21]. Compared to existing cellular materials, the lattice metamaterials exhibited quite competitive mechanical properties in compressive modulus and strength. Despite numerous efforts devoted to this exuberant field, ultralightweight mechanical metamaterials with combined high strength and superior energy absorption remain poorly reported. To address this deficiency, we recently proposed a novel ultralightweight hierarchical origami-corrugation *meta*-sandwich (HOCM) structure with superior out-of-plane compressive mechanical properties, including strength and energy absorption [22]. The HOCM structures fabricated using the technique of selective laser melting (SLM) were evaluated with quasi-static out-of-plane compressive tests. The results confirmed that both the compressive strength and energy absorption were improved significantly. Physical mechanisms underlying such superior mechanical response were also explored and the effects of parent material make discussed. Nonetheless, these remarkable results were attained without systematic geometry parametric analysis. In total, there are 9 independent geometric parameters in a HOCM structure and how these parameters affect its mechanical properties remains elusive. Therefore, exploring the critical influence of geometric parameters and then establishing an efficient optimization strategy is of great significance for in-depth understanding and promotion of the proposed HOCM structures.

For a complex structure like the HOCM, the relationship between its mechanical performance and geometric parameters is often too non-smooth and nonlinear to derive either analytical or empirical solutions [23], thus limiting significantly its optimal design for specific practical applications. Recently, surrogate modeling based on machine learning (ML) has drawn great attention, especially for those struggling in solving complicated engineering problems with traditional methods, due mainly to its promising substitute for analytical and empirical solutions. For instance, based on ML models such as regression trees and neural networks (NNs), a new class of solutions was proposed for fracture mechanics problems [24]. It was found that while both models could provide accurate results for specific problems, the NN-based solutions outperform regression-tree-based solutions in terms of simplicity. Based on a neural network algorithm depending on plastic strain, strain rate, and temperature, a modified Johnson-Cook plasticity model was proposed to capture the plastic and fracture behaviors of dual-phase steels [25]. The work demonstrated that, with machine learning, a hardening law can be identified using a hybrid experimental–numerical analysis, without adding any model bias before calibration. A machine learning based model was then proposed to describe the temperature and strain rate dependent response of polypropylene, and its capability to efficiently predict experimentally observed stress–strain response was demonstrated [26]. Therefore, the method of machine learning has great potential for surrogate modeling to approximate and predict complex and/or nonlinear problems.

Moreover, incorporating surrogate modeling with optimization algorithms has promoted the optimization efficiency of multi-objective engineering design [27], for it could reduce the computational effort for simulation as well as avoid the difficulty of expressing highly nonlinear relations by exact equations [28]. The multi-objective optimization is of great potential and efficiency in energy absorption [28] or multi-functional application scenarios [29–31] and thus is widely employed in these fields. Recently, several studies about tubing energy absorption have been conducted based on multi-objective optimization for peak forces and energy absorption, which greatly reduced design time for energy absorption devices [32–36]. A multi-objective optimization was also employed to perform blast-resistant design of sandwich structures based on the Kriging surrogate modeling: the optimal design from the Pareto front was found to be quite efficient in lightweight and blast resistance [37]. Three types of optimal design for metallic corrugated sandwich panels with polyurea-metal laminate face sheets were subsequently compared to seek the trade-off design of stiffness and vibration damping [38]. Many other fields have also been performed with the multi-objective optimization, for example, diffuse field sound transmission loss on the lightweight shell composite sandwich structures [39], plane sound wave transmission loss on the lightweight laminated composite cylindrical shell [40], and so on.

In the present study, inspired by the aforementioned knowledge gaps, the out-of-plane compressive performances of novel HOCM structures proposed recently by us are systematically investigated theoretically, experimentally, and numerically. Firstly, an analytical model to predict the equivalent elastic constants of the *meta*-mechanical structure is established. Secondly, out-of-plane compression experiments are carried out with SLM printed HOCM samples. Thirdly, a representative volume element (RVE) model of finite element (FE) simulations is proposed to explore further the compressive performance and the underlying physical mechanisms. Subsequently, built upon the fully connected neural network algorithm, a machine-learning-based surrogate model is developed to approximate the specific peak strength (SPS) and specific energy absorption (SEA) of HOCM structures. Finally, upon incorporation with the surrogate model, the non-dominated sorting genetic algorithm II is selected to carry out multi-objective optimization for simultaneous superior SPS, SEA with assured stiffness.

2. Analytical model of elastic constants

2.1. Geometry of HOCM structure

The proposed HOCM structure is inspired by the Miura-Ori structure. As illustrated in Fig. 1, the unit cell of HOCM consists of four inclined parallelogram corrugated sandwich plates. Let a and b represent the length of two edges of an inclined corrugated sandwich plate, c the length of the edge of corrugation platform, α' the angle between the inclination edge and horizontal line of parallelogram plates, β the folding angle, and φ the acute angle of parallelogram plates. The parametersα', β and φ are related by:

$$\cos\varphi = \cos\alpha' \cdot \cos\beta, \tag{1}$$

$$\sin^2\varphi = \sin^2\alpha' + \cos^2\alpha' \cdot \sin^2\beta. \tag{2}$$

To reveal the geometric information of internal corrugations, a cross-section is set in the HOCM structure as shown in Fig. 1, with the inner geometrical morphology of corrugations enlarged with corresponding parameters marked on it. The inner corrugations are characterized by the inclination angle γ, strut (corrugations web) thicknesst_1, strut lengthl_1, and half wavelength s. The overall parameters of the HOCM structure are related to the corrugation parameters by:

$$\tan\alpha' = \tan\alpha \cdot \sin\beta, \tag{3}$$

$$w = c \cdot \sin\beta = \frac{2(l_1 \cdot \sin\gamma + 2t + t_1)}{\sin\alpha}, \tag{4}$$

$$l = b \cdot \sin\varphi, \tag{5}$$

where α and l are the inclination angle and the height of parallelogram plates, respectively, and w is the width of corrugation platform in the cross-section.

Based on parameter relationships described above, the HOCM

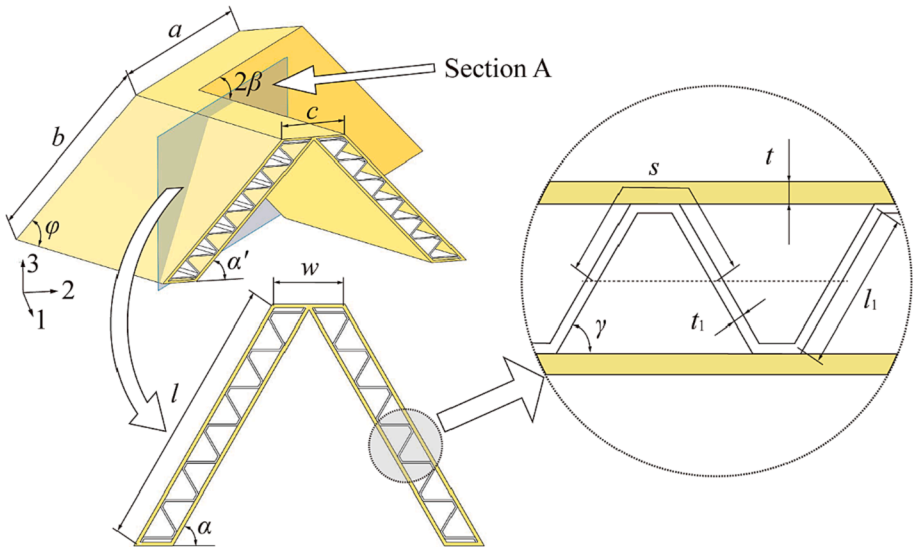

Fig. 1. Schematic of hierarchical origami-corrugation *meta*-sandwich (HOCM) structure.

structure is determined by 9 independent parameters, namely, a, l, t, l_1, t_1, s, α, β and γ, and its relative density $\bar{\rho}$ can be expressed as:

$$\bar{\rho} = \frac{2\left\{2lt + lt_1\left[\frac{s}{s+(\cos\gamma-1)l_1}\right] + \frac{2(l_1\cdot\sin\gamma+2t+t_1)t}{\sin\alpha}\right\}}{l[a\cdot\sin\alpha\cdot\sin\beta\cdot\cos\beta + 2l\cdot\sin\alpha\cdot\cos\alpha + 2(l_1\cdot\sin\gamma + 2t + t_1)]}. \quad (6)$$

2.2. Analytical model

In this section, a theoretical model to predict the equivalent elastic constants of HOCMs is established. It is of great significance to reveal the elastic behavior of HOCMs. In the later section, the analytical model is validated by the FE simulations. In addition, for the multi-objective optimal design, the compressive stiffness of HOCMs is set as the critical constraint, to guarantee the deformation resistibility at linear elastic stage of optimal results.

2.2.1. Simplifications and assumptions

To simplify the derivation process, several basic assumptions are made:

(1) The whole HOCM structure is perfect in geometry (i.e., without any internal defects) and made of the same isotropic parent material.

(2) The structure can be homogenized within its representative volume unit and hence can be taken as a fictive homogeneous bulk material.

(3) The corrugated sandwich plates forming the parallelogram facet are taken as equivalent orthotropic plates, and only in-plane stresses in these plates are considered when analyzing the compressive behavior of the HOCM structure.

(4) Elastic compression under small deformation is analyzed based on the assumption of linear elasticity.

Given the hierarchical feature of the HOCM structure, a two-level homogenization approach is developed, i.e., the first-level homogenization for corrugated sandwich plates, and the second-level homogenization for the Miura-Ori foldcore consisting of inclined parallelogram facets.

With reference to Fig. 2**a**, the unit cell of a HOCM structure is placed in the global coordinate system O-xyz. Meanwhile, the Cartesian coordinate system O-$\eta'\xi'\theta'$ is set based on the inclined parallelogram facet, with the base vectors defined as $\boldsymbol{e}_{i'}$ (i = 1, 2, 3), whose inverse basis vectors are $\boldsymbol{e}^{i'}$ (i = 1, 2, 3).

Due to structural symmetry of two adjacent parallelogram facets, only one inclined parallelogram made of corrugated sandwich plate needs to be analyzed. Fig. 2**b** presents the in-plane stresses and mechanical model for such an inclined parallelogram facet. The coordinate system $\eta O\xi$ is set along the parallelogram edges, whose base vectors are $\boldsymbol{g}_i$ (i = 1, 2), with the inverse vectors defined as $\boldsymbol{g}^i$ (i = 1, 2).

2.2.2. Stiffness model of corrugated sandwich plate

First-level homogenization for corrugated sandwich plate: Each corrugated sandwich plate is constituted of two face sheets and a corrugated core. For the corrugated core, the stiffness in longitudinal and transverse directions are not the same: as shown in Fig. 2, the longitudinal direction is the direction of corrugated channels along$O\eta'$, while the transverse direction is the periodic direction of corrugations along$O\xi'$. Therefore, the corrugated core can be treated as an equivalent orthotropic plate,

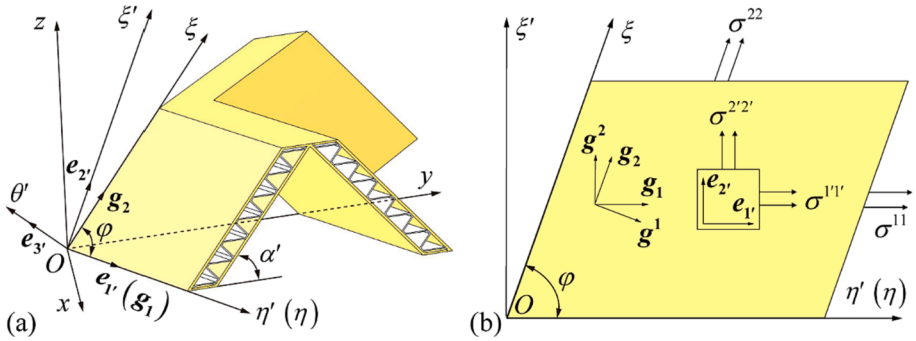

Fig. 2. Mechanical model of HOCM structure: (a) coordinate systems and (b) in-plane stresses and mechanical model of inclined parallelogram facet.

such that its stress versus strain relationship can be written as:

$$\begin{Bmatrix} \sigma^{1'1'} \\ \sigma^{2'2'} \\ \sigma^{1'2'} \end{Bmatrix}_{\text{eop}} = \begin{bmatrix} A^{1'1'1'1'} & A^{1'1'2'2'} & 0 \\ A^{2'2'1'1'} & A^{2'2'2'2'} & 0 \\ 0 & 0 & A^{1'2'1'2'} \end{bmatrix}_{\text{eop}} \begin{Bmatrix} \varepsilon_{1'1'} \\ \varepsilon_{2'2'} \\ \varepsilon_{1'2'} \end{Bmatrix}_{\text{eop}}, \tag{7}$$

where $A^{1'1'2'2'}$ is equal to $A^{2'2'1'1'}$, and the subscript "eop" represents the equivalent orthotropic plate.

Based on the principle of energy equivalence, the extensional rigidity of a trapezoidal corrugated core had been derived, as [41,42]:

$$A^{1'1'1'1'} = E\frac{s}{s + l_1(\cos\gamma - 1)}, \tag{8}$$

$$A^{2'2'2'2'} = \frac{Et_1^2[s + l_1(\cos\gamma - 1)]}{(3s - 2l_1)l_1^2\sin^2\gamma}, \tag{9}$$

$$A^{1'1'2'2'} = \nu A^{2'2'2'2'}, \tag{10}$$

$$A^{1'2'1'2'} = \frac{E[s + l_1(\cos\gamma - 1)]}{2s(1+\nu)}, \tag{11}$$

where E and ν are Young's modulus and Poisson ratio of the parent material made into the corrugated core.

As for the two face sheets of the corrugated sandwich plate, the stress versus strain relationship can be written as:

$$\begin{Bmatrix} \sigma^{1'1'} \\ \sigma^{2'2'} \\ \sigma^{1'2'} \end{Bmatrix}_{\text{fs}} = \begin{bmatrix} \frac{E}{1-\nu^2} & \frac{\nu E}{1-\nu^2} & 0 \\ \frac{\nu E}{1-\nu^2} & \frac{E}{1-\nu^2} & 0 \\ 0 & 0 & \frac{E}{2(1+\nu)} \end{bmatrix}_{\text{fs}} \begin{Bmatrix} \varepsilon_{1'1'} \\ \varepsilon_{2'2'} \\ \varepsilon_{1'2'} \end{Bmatrix}_{\text{fs}}, \tag{12}$$

where the subscript "fs" represents the face sheets.

Based on the well-established mechanics of composite materials, the extensional rigidity of a laminate can be derived by linear superposition. Therefore, with the corrugated sandwich plate taken as a three-layer laminate, its in-plane stress versus strain relationship can be derived as:

$$\begin{Bmatrix} \sigma^{1'1'} \\ \sigma^{2'2'} \\ \sigma^{1'2'} \end{Bmatrix} = \begin{bmatrix} B^{1'1'1'1'} & B^{1'1'2'2'} & 0 \\ B^{2'2'1'1'} & B^{2'2'2'2'} & 0 \\ 0 & 0 & B^{1'2'1'2'} \end{bmatrix} \begin{Bmatrix} \varepsilon_{1'1'} \\ \varepsilon_{2'2'} \\ \varepsilon_{1'2'} \end{Bmatrix}, \tag{13}$$

or, expressed in tensor form, as:

$$\sigma^{i'\,j'} = B^{i'\,j'\,k'\,l'}\varepsilon_{k'\,l'}, \tag{14}$$

here, $B^{i'\,j'\,k'\,l'}$ is the extensional rigidity of the corrugated sandwich plate, given by:

$$B^{1'1'1'1'} = \frac{2tE + (1-\nu^2)t_1A^{1'1'1'1'}}{(2t + t_1)(1-\nu^2)}, \tag{15}$$

$$B^{2'2'2'2'} = \frac{2tE + (1-\nu^2)t_1A^{2'2'2'2'}}{(2t + t_1)(1-\nu^2)}, \tag{16}$$

$$B^{1'1'2'2'} = B^{2'2'1'1'} = \frac{2t\nu E + (1-\nu^2)t_1\nu A^{2'2'2'2'}}{(2t + t_1)(1-\nu^2)}, \tag{17}$$

$$B^{1'2'1'2'} = \frac{tE + (1+\nu)t_1A^{1'2'1'2'}}{(2t + t_1)(1+\nu)}. \tag{18}$$

2.2.3. Equivalent elasticity coefficients

Second-level homogenization for inclined parallelogram facet in Miura-Ori foldcore: Fig. 2**b** displays the directions of the rectangular coordinate system $\eta'O\xi'$ and the inclined coordinate system $\eta O\xi$, together with their base and inverse base vectors. The base and inverse base vectors of the rectangular coordinate system are $\boldsymbol{g}_i$ and $\boldsymbol{g}^i$, while those for the inclined coordinate system are $\boldsymbol{e}_{i'}$ and $\boldsymbol{e}^{i'}$ respectively. Note that, via a rigid body rotation, $\boldsymbol{g}_i$ and $\boldsymbol{g}^i$ can be made to coincide with $\boldsymbol{e}_{i'}$ and $\boldsymbol{e}^{i'}$. Namely, they can be related by the orthogonal tensor, as:

$$\boldsymbol{e}_{i'} = \boldsymbol{\beta}_{i'}^{j}\boldsymbol{g}_j \tag{19}$$

$$\boldsymbol{g}^k = \boldsymbol{\beta}_{l'}^{k}\boldsymbol{e}^{l'} \tag{20}$$

where i, j, k, l = 1, 2.

The rules of coordinate transformation dictate that the stresses and strains in the rectangular coordinate system $\eta'O\xi'$ and the inclined coordinate system $\eta O\xi$ are related by:

$$\sigma^{ij} = \beta_{i'}^{i}\beta_{j'}^{j}\sigma^{i'\,j'}, \tag{21}$$

$$\varepsilon_{k'\,l'} = \beta_{k'}^{k}\beta_{l'}^{l}\varepsilon_{kl}, \tag{22}$$

where σ^{ij} and ε_{kl} are the stress and strain in the inclined coordinate system $\eta O\xi$, while $\sigma^{i'\,j'}$ and $\varepsilon_{k'\,l'}$ are the stress and strain in the rectangular coordinate system $\eta'O\xi'$.

For the corrugated sandwich plate, the stress versus strain relationship in the inclined coordinate system $\eta O\xi$ can be written as:

$$\begin{Bmatrix} \sigma^{11} \\ \sigma^{22} \\ \sigma^{12} \end{Bmatrix} = \begin{bmatrix} B^{1111} & B^{1122} & 0 \\ B^{2211} & B^{2222} & 0 \\ 0 & 0 & B^{1212} \end{bmatrix} \begin{Bmatrix} \varepsilon_{11} \\ \varepsilon_{22} \\ \varepsilon_{12} \end{Bmatrix}, \tag{23}$$

or.

$$\sigma^{ij} = B^{ijkl}\varepsilon_{kl}. \tag{24}$$

Substituting Eqs. (21) and (22) into Eq. (24) leads to the stress versus strain relationship expressed in the inclined coordinate system $\eta O\xi$, as:

$$\sigma^{ij} = \beta_{i'}^{i}\beta_{j'}^{j}B^{i'\,j'\,k'\,l'}\beta_{k'}^{k}\beta_{l'}^{l}\varepsilon_{kl}. \tag{25}$$

Comparing Eq. (24) and Eq. (25) yields:

$$B^{ijkl} = \beta_{i'}^{i}\beta_{j'}^{j}B^{i'\,j'\,k'\,l'}\beta_{k'}^{k}\beta_{l'}^{l}, \tag{26}$$

or, in matrix form:

$$[\boldsymbol{B}] = [\boldsymbol{T}][\boldsymbol{B}'][\boldsymbol{Q}] \tag{27}$$

where.

$$[\boldsymbol{T}] = \begin{bmatrix} \beta_{1'}^{1}\beta_{1'}^{1} & \beta_{2'}^{1}\beta_{2'}^{1} & \beta_{1'}^{1}\beta_{2'}^{1} \\ \beta_{1'}^{2}\beta_{1'}^{2} & \beta_{2'}^{2}\beta_{2'}^{2} & \beta_{1'}^{2}\beta_{2'}^{2} \\ \beta_{1'}^{1}\beta_{1'}^{2} & \beta_{2'}^{1}\beta_{2'}^{2} & \beta_{1'}^{1}\beta_{2'}^{2} \end{bmatrix} = \begin{bmatrix} 1 & \cot^2\varphi & -\cot\varphi \\ 0 & \csc^2\varphi & 0 \\ 0 & -\cot\varphi\cdot\csc\varphi & \csc\varphi \end{bmatrix}, \tag{28}$$

$$[\boldsymbol{Q}] = \begin{bmatrix} \beta_{1'}^{1}\beta_{1'}^{1} & \beta_{2'}^{1}\beta_{2'}^{1} & \beta_{1'}^{1}\beta_{1'}^{2} \\ \beta_{2'}^{1}\beta_{2'}^{1} & \beta_{2'}^{2}\beta_{2'}^{2} & \beta_{2'}^{1}\beta_{2'}^{2} \\ \beta_{1'}^{1}\beta_{2'}^{1} & \beta_{1'}^{2}\beta_{2'}^{2} & \beta_{1'}^{1}\beta_{2'}^{2} \end{bmatrix} = \begin{bmatrix} 1 & 0 & 0 \\ \cot^2\varphi & \csc^2\varphi & -\cot\varphi\cdot\csc\varphi \\ -\cot\varphi & 0 & \csc\varphi \end{bmatrix}. \tag{29}$$

Substitution of Eqs. (28) and (29) into Eq. (27) results in:

$$B^{2222} = B^{2'2'2'2'}\csc^4\varphi. \tag{30}$$

2.2.4. Compressive modulus

According to the rules of coordinate transformation, the strains in the global coordinate system *O-xyz* are related to those in the inclined coordinate system $\eta O\xi$:

$$\varepsilon_{mn} = \beta_{m}^{m*}\beta_{n}^{n*}\varepsilon_{m*n*}, \tag{31}$$

where m, n = 1, 2, 3, and $m*$, $n* = x, y, z$.

When the HOCM structure is subjected to out-of-plane compression

along the z-axis direction (the displacement components:$U = V = 0, W \neq 0$; U, along the x-axis direction, V, along the y-axis direction, and W, along the z-axis direction), the equivalent strains could be written by:

$$\begin{cases} \varepsilon_{zz} = \dfrac{W}{h} \\ \varepsilon_{zx} = \varepsilon_{zy} = 0 \end{cases}. \tag{32}$$

Therefore, according to the stress versus strain relationship established above, the corresponding equivalent stresses are:

$$\begin{cases} \sigma^{zz} = E^{zzzz}\varepsilon_{zz} \\ \sigma^{zx} = \sigma^{zy} = 0 \end{cases}. \tag{33}$$

Within the equivalent volume of the unit cell, the average stresses on a cross-section ($x = \text{const}, y = \text{const}, z = \text{const}$) are$\sigma^{zx}$, σ^{zy} andσ^{zz}. The potential strain energy can be calculated by:

$$\Pi = \frac{1}{2}\iiint_V \boldsymbol{\sigma}\boldsymbol{\varepsilon}\mathrm{d}V = \frac{1}{2}\iiint_{V_e} \sigma^{m*n*}\varepsilon_{m*n*}\mathrm{d}V, \tag{34}$$

where V_e is the equivalent volume of the unit cell (i.e., the volume of circumscribed cuboid of the HOCMs' unit cell), given by:

$$V_e = 2ab{\cdot}\sin\alpha^{'}{\cdot}\sin\beta(a{\cdot}\cos\beta + 2b{\cdot}\cos\alpha^{'} + c) \tag{35}$$

Substituting Eqs. (33) and (35) into Eq. (34) leads to:

$$\Pi = ab{\cdot}\sin\alpha^{'}{\cdot}\sin\beta(a{\cdot}\cos\beta + 2b{\cdot}\cos\alpha^{'} + c)E^{zzzz}\varepsilon_{zz}^2. \tag{36}$$

Based on Eq. (31), the in-plane strains of the parallelogram wall shown in Fig. 2**b** can be derived as:

$$\begin{cases} \varepsilon_{22} = \sin^2\alpha^{'}{\cdot}\varepsilon_{zz} \\ \varepsilon_{11} = \varepsilon_{12} = \varepsilon_{21} = 0 \end{cases}. \tag{37}$$

Assume that the parallelogram wall is in-plane stress state, and only in-plane stresses and small elastic deformation are considered. The strain energy $\Pi^{'}$ within the parallelogram wall in the inclined coordinate system $\eta O\xi$ can be written as:

$$\Pi^{'} = \frac{1}{2}\iiint_V \boldsymbol{\sigma}\boldsymbol{\varepsilon}\mathrm{d}V = \frac{1}{2}\iiint_V \sigma^{mn}\varepsilon_{mn}\mathrm{d}V, \tag{38}$$

where V is the volume of the parallelogram wall, given by:

$$V = 2ab(2t + t_1)\sin\varphi. \tag{39}$$

Substitution of Eqs. (24), (37) and (39) into Eq. (38) yields:

$$\Pi^{'} = \frac{1}{2}ab(2t + t_1)\sin\varphi{\cdot}\sin^2\alpha^{'}{\cdot}B^{2222}\varepsilon_{zz}^2. \tag{40}$$

Based on the principle of work equivalence for the walls of the unit cell, one has:

$$\Pi = 4\Pi^{'}. \tag{41}$$

Finally, upon substituting Eqs. (30), (36) and (40) into Eq. (41), the equivalent compressive modulus of a HOCM structure under quasi-static compression along the z-axis direction (Fig. 2) is derived, as:

$$E^{zzzz} = \frac{2(2t + t_1)\sin^3\alpha^{'}{\cdot}\csc^3\varphi{\cdot}B^{2^{'}2^{'}2^{'}2^{'}}}{\sin\beta{\cdot}(a\cos\beta + 2b\cos\alpha^{'} + c)}. \tag{42}$$

3. Experiments

3.1. Materials and fabrication methodology

In contrast to steel and aluminum alloys, the Inconel alloy IN718 possesses higher specific strength and service temperature, thus great potential for applications in extreme environments [43]. The IN718 material is selected as the parent material for all HOCM test samples fabricated in the present study.

Additive manufacturing (AM) of metallic materials provides attractive benefits to the fabrication of complex geometry structures [44]. To guarantee the manufacturing quality, the HOCM samples are fabricated using the selective laser melting (SLM) AM technique.

Table 1 lists the geometric dimensions of as-fabricated HOCM test samples. Three different wall thickness values are selected to investigate the effect of relative density, and each sample contains two unit cells. The IN718 metallic powders used for SLM are in good spheroidization, with particle sizes varying between 5 μm and 50 μm. Chemical composition of the powders is listed in Table 2. As for the technical parameters of SLM, the skin layer is printed with a laser power of 75 W and a scanning speed of 800 mm/s while the inner region is printed with a laser power of 305 W and a scanning speed of 960 mm/s, such that the fabricated samples can be easily removed from the workbench.

Fig. 3 presents photographs of the three test samples detailed in Table 1. The quality of sample fabrication is evaluated with scanning electron microscopy (SEM, SU3500, Hitachi, Japan). Fig. 3**b** displays the SEM image of the outside surface region marked in Fig. 3**a** by white dashed line A. The outside surface of the sample is seen to be relatively flat with no presence of holes, thus indicating good manufacturing quality. For the observation of the inner region, the sample is cut along the white dashed line B shown in Fig. 3**a** via wire-cut electro-discharge machining (EDM) then the inner face is magnified through SEM, as shown in Fig. 3**c**. The interior of the sample is relatively dense, with only a small amount of un-melted metal powders (marked by black dashed line) observed. In all, the test samples fabricated via SLM exhibit only a few minor defects.

To characterize the mechanical properties of the parent material (IN718), room temperature uniaxial quasi-static tensile tests are conducted on an MTS machine (MTS-858 Mini bionix, MTS Corporation, USA), with a nominal strain rate of 1×10^{-3} s^{-1}. Dog-bone samples are designed and manufactured using the SLM technique, with identical printing parameters as those adopted for HOCM samples. Force and displacement profiles are generated by the testing machine and recorded by an extensometer simultaneously. A total of six nominally identical samples are tested, and the resulting average true stress versus true strain curve is shown in Fig. 4. Generally speaking, the IN718 manufactured by SLM exhibits a typical elastic-linearly hardening behavior, with density $\rho = 8240$ kg/m^3, Young's modulus $E = 144.51$ GPa, and 0.2% offset yield strength$\sigma_{0.2} = 815.16$ MPa.

3.2. Experimental measurements

Quasi-static out-of-plane compressive responses of the HOCM samples are measured with a hydraulic testing machine (MTS). Fig. 5 displays the experimental set-up, which is consisted of upper and lower platens, a floodlight, and a digital video. While the lower platen is fixed, the upper platen is set to apply a compressive load along the 3-direction (i.e., out-of-plane direction) by moving down with a fixed nominal strain rate of 5.96×10^{-4} s^{-1}. With the floodlight adopted to improve ambient brightness, a digital video is set at the side of each test sample along the 1-direction (Fig. 5) to record its deformation details. The force and displacement profiles are generated by the testing machine synchronously.

3.3. Experimental results

Quasi-static out-of-plane compressive responses of the tested HOCM samples are presented in Fig. 6. The nominal strain is calculated as the ratio of displacement and sample height, while the nominal stress as the ratio of compressive loading force and sample cross-sectional area in accordance with the ASTM STP C365. As shown in Fig. 6**a**, sample T1 exhibits an initial linear compressive response till a peak strength is reached, followed by a sudden and dramatic drop before reaching a long-term stress plateau with slight fluctuations till densification.

To investigate the effect of relative density, samples T2 and T3 are

Table 1
Geometric parameters of HOCM samples fabricated by SLM and tested in the current study.

Sample No.	a (mm)	l (mm)	l_1 (mm)	t (mm)	t_1 (mm)	s (mm)	α	β	γ	$\bar{\rho}$
T1	20	27.24	6	**0.60**	**0.60**	6	67.79°	45°	60°	**0.124**
T2	20	27.24	6	**0.74**	**0.74**	6	67.79°	45°	60°	**0.152**
T3	20	27.24	6	**0.95**	**0.95**	6	67.79°	45°	60°	**0.194**

Table 2
Chemical composition of IN718 powders for SLM fabrication (unit: wt.%).

IN718	Ni	Cr	Nb	Mo	Ti	Al	C	Si & Mn & Cu	Fe
	50 ~ 55	17 ~ 21	4.75 ~ 5.5	2.8 ~ 3.3	0.65 ~ 1.15	0.2 ~ 0.8	≤0.08	≤0.35	Bal.

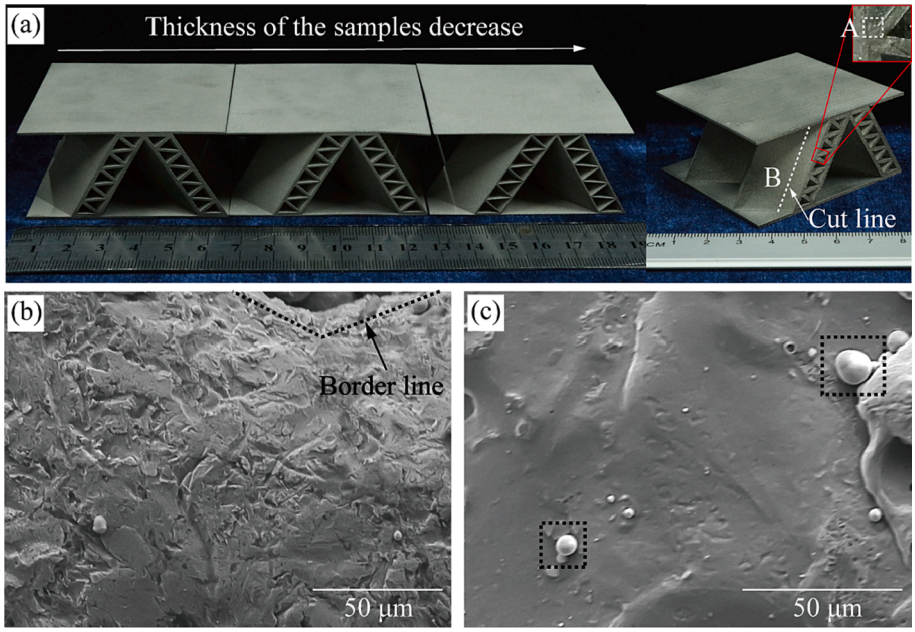

Fig. 3. HOCM test samples fabricated via SLM: (a) photographs of three samples listed in Table 1, (b) SEM image of outside surface A marked in (a), and (c) SEM image of inner surface cut by electric spark wire B marked in (a).

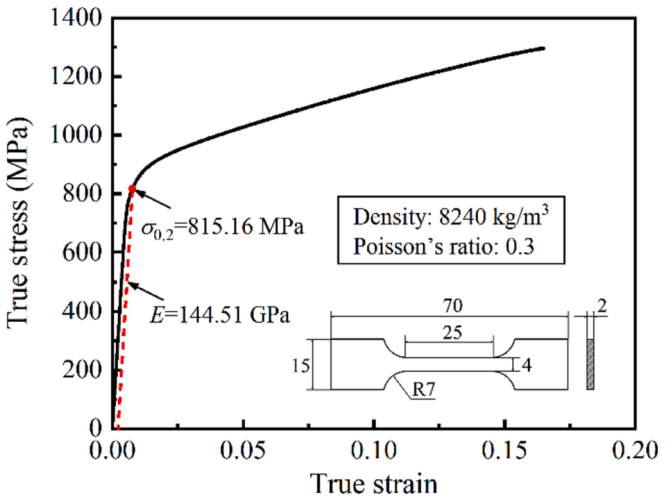

Fig. 4. Measured tensile true stress versus true strain curve of IN718 fabricated via SLM.

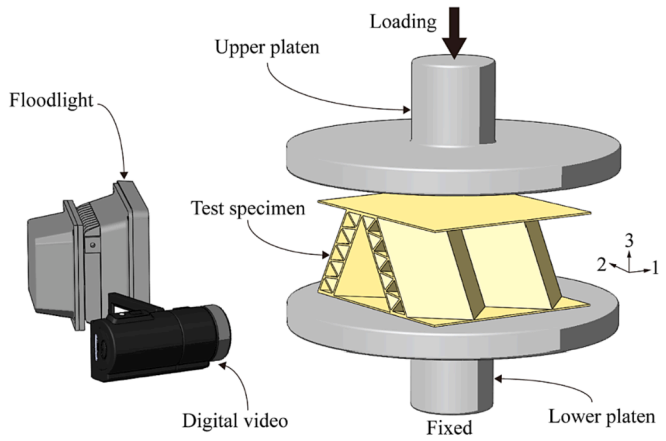

Fig. 5. Schematic of hierarchical origami sandwich specimen under quasi-static out-of-plane compression.

measured, with the relative density gradually increased (relative to T1) by changing the wall thickness, as detailed in Table 1. As shown in Fig. 6**b and c**, two experiments (EXP1 and EXP2) are conducted with each type of sample: excellent match is achieved between EXP1 and

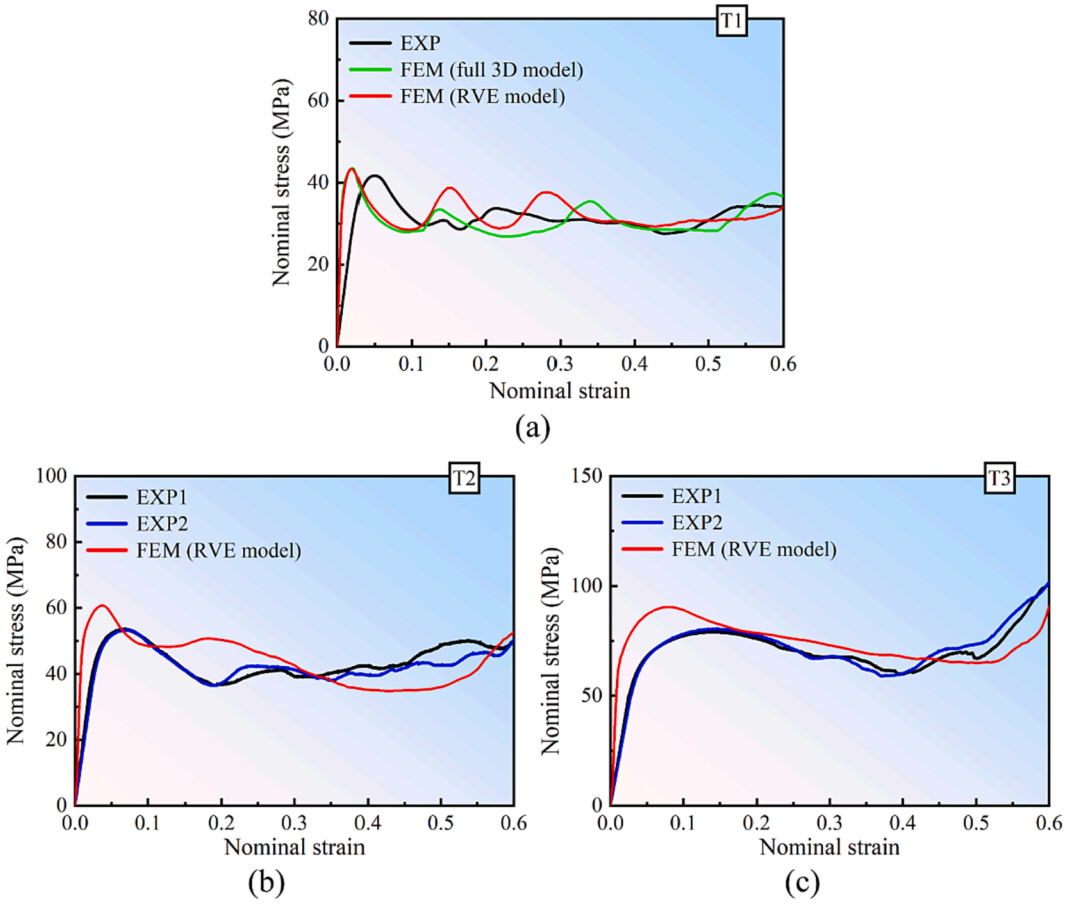

Fig. 6. Out-of-plane compressive strain versus stress curves of HOCM samples obtained from both experiments and simulations: (a) T1, (b) T2 and (c) T3.

EXP2, indicating excellent consistency in manufacturing quality. Compared with the compressive curve of T1, the downtrend after the peak strength is softened for both T2 and T3. For T2, the downtrend of the curve is softened slightly, whereas for T3 it is almost impossible to distinguish the drop segment of the curve from the platform segment. In addition, as wall thickness (relative density) is increased, fluctuations in the platform segment become less significant.

Table 3 summarizes the measured values of peak strength and energy absorption (defined as the area of nominal strain versus stress curve from strain 0 to 0.5) for samples T1, T2 and T3. Both the peak strength and energy absorption increase with increasing relative density. Further, the results of Tables 1 and 3 reveal a nonlinear increase: in contrast to T1, the relative density of T2 is increased by 22.58% while its peak strength and energy absorption are increased by 28.67% and 35.13%, respectively; however, compared with T2, the relative density of T3 is increased by 27.63% while its peak strength and energy absorption are increased by 49.32% and 62.66%, respectively.

Fig. 7 displays the deformation configurations of sample T1 at ε_n = 0.65; similar deformation patterns are found in T2 and T3 and hence not shown here for brevity. Pile-up wrinkling layer by layer can be observed, which is induced mainly by the introduction of corrugations. Some inner corrugations produce local buckling as well, which accumulates with the wrinkling of outer panels. Further, there exists an overall buckling deformation mode, annotated by red dotted line in Fig. 7. Only a few cracks can be found on the folds, which benefit from the decent ductility of IN718.

4. Numerical simulation

4.1. Finite element model

Finite element (FE) simulations of HOCM structures under quasi-static out-of-plane compression are carried out with the commercially available ABAQUS v6.16/Explicit. The geometric parameters are iden-

Table 3
Compressive peak strength and energy absorption of HOCM samples: comparison between experimental measurements and simulation results.

Sample No.	Peak strength (MPa)				Energy absorption (MJ/m^3)			
	EXP	FEM		Errors (%)	EXP	FEM		Errors (%)
		Full 3D model	RVE model			Full 3D model	RVE model	
T1	41.68	43.49	43.39	4.10	15.40	15.15	15.86	2.99
T2	53.63	–	60.81	13.39	20.81	–	21.96	5.53
T3	80.08	–	90.44	12.94	33.85	–	37.22	9.96

Note: energy absorption is defined as the area of crushing nominal strain versus stress curve from strain 0 to 0.5; EXP and FEM refer to experimentally measured and numerically calculated results; for samples T2 and T3, the value of EXP is the average of two experiments; the errors are calculated from the experimental measurements and the RVE model simulated results.

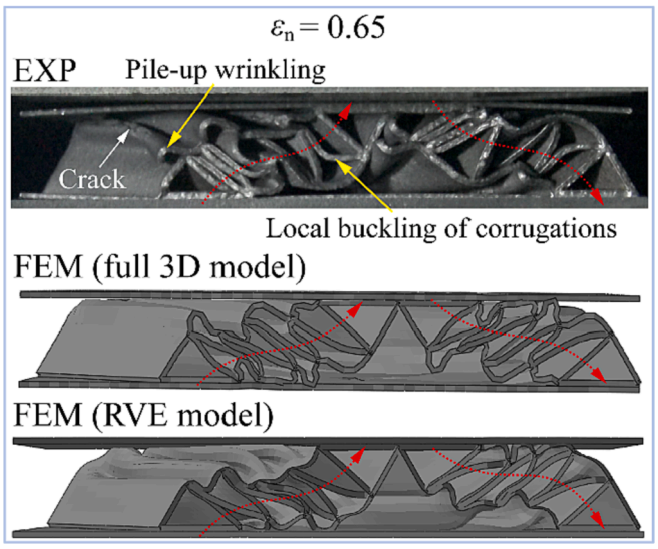

Fig. 7. Deformation configurations of sample T1: comparison between experiment and simulations.

tical to those of experimentally tested samples, with small geometric imperfections induced during fabrication ignored. Two rigid plates are used to model the upper and lower platens. Due to symmetry in both sample geometry and loading condition, only a quarter of each sample (half of a unit cell) with symmetric boundaries is considered in the simulations as shown in Fig. 8 (defined as the representative volume element, RVE). As a reference, full three-dimensional (3D) models with the same dimensions as tested samples are also considered. Four-node shell elements (S4R) with five integration points through the thickness are used to model the HOCM structure, while the loading platens are meshed with four-node rigid elements (R3D4). Upon performing a mesh sensitivity study for balanced numerical accuracy and computational cost (results not shown here for brevity), the average mesh size for both the HOCM structure and rigid platens is selected as $l_1/8$.

General contact is employed for all the models, with a fixed Coulomb friction coefficient of 0.3. Based on the tie constraint algorithm, interfaces between the corrugations and the original Miura-Ori facets are bonded ideally. With the bottom rigid plate fixed, axial displacement loading is applied on the top rigid plate at a sufficiently slow speed to mimic quasi-static compression.

Based on the tensile test illustrated in Fig. 4, the parent material (IN718) is modeled as an isotropic elastic–plastic solid governed by the von Mises J2 flow theory, without material damage considered. The elastic behavior is modeled using the parameters summarized in Fig. 4, while the plastic behavior is simulated by inputting the measured true strain versus stress data.

4.2. Validation

The compressive responses of samples T1 ~ T3 are calculated numerically and compared with those experimentally measured in Fig. 6, with good agreement achieved. Note that the numerical results calculated based on both the full 3D model (Fig. 8**a**) and RVE model (Fig. 8**b**) are presented in Fig. 6**a**. The compressive strain versus stress curves of both models are almost the same, except for a slight difference in the stress plateau region. Since it is difficult to accurately measure the compressive modulus in experiments, the numerically calculated compressive modulus for each sample is compared with that predicted by the analytical model developed in **Section 2.2**. As shown in Table 4, the errors between analytical predictions and FE simulations are quite small (all less than 7%), thus validating the effectiveness of the proposed analytical model. Moreover, the peak compressive stress and energy absorption from experiments and simulations are summarized in Table 3. For samples T2 and T3, the experimental results are the average values of two separate measurements. It is shown that the errors between experimental and numerical results are all below 14%. Specifically, these slight differences are mainly attributed to the following reasons: (1) the platens are modeled as rigid plates, without regard to the flexibility of platens and contact stiffness of the testing machine; (2) the ideally regular geometry of samples is modeled ignoring the defects induced during the fabrication; (3) the inevitable randomness of contact regions in the compressive process may cause the slight mismatch of the fluctuations in the plateau region of the stress–strain curves; (4) the reasonable simplification of the RVE model using symmetric boundaries might differ slightly from the real experiments. Overall, the present RVE

Table 4
Equivalent compressive moduli of HOCM samples: comparison between analytical model predictions and FE simulation results.

Sample No.	Equivalent compressive modulus (GPa)		Error (%)
	Ana.	FEM (RVE model)	
T1	6.64	6.40	3.61
T2	8.04	7.59	5.60
T3	10.06	9.42	6.36

Note: Ana. and FEM refer to analytical predictions and FE calculations, respectively.

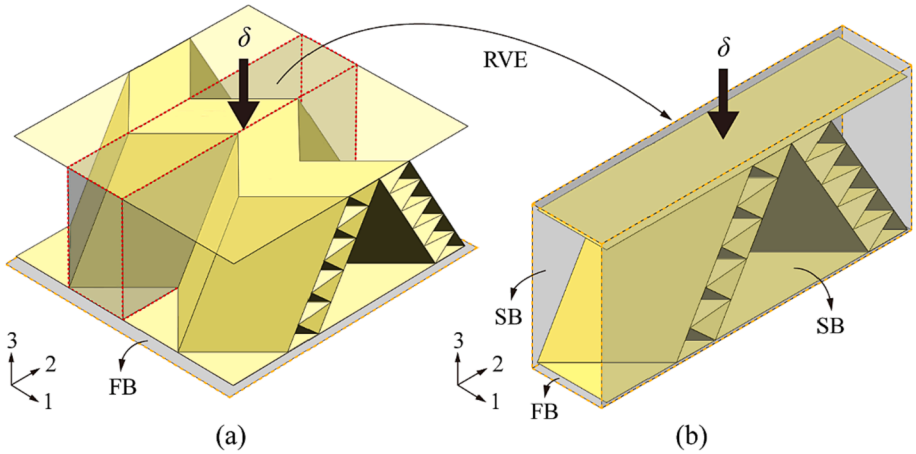

Fig. 8. Schematic of FE model for numerical simulations: (a) full three-dimensional (3D) model and (b) representative volume element (RVE) model; SB: symmetric boundary, FB: fixed boundary.

model can mimic the compressive performance of a HOCM structure quite well.

5. Parametric study

Thus far, the equivalent compressive modulus of the proposed HOCM structure has been analytically derived while its compressive response has been measured as a function of relative density, with promising potential for applications requiring simultaneous load-bearing and energy absorption at ultralightweight. Meanwhile, the nonlinear effects of relative density have been observed through experiments. Further, the FE-based RVE numerical models were used to simulate the compressive responses, with reasonable agreement achieved among FE simulation results, analytical predictions and experimental measurements. In this section, the validated FE method is employed to quantify the effects of two non-dimensional parameters, i.e., the slenderness ratio p_1 ($=l/l_1$) and wall thickness ratio p_2 ($=t/t_1$), and two angle parameters, i.e., the folding angles α and β. To expand the discussion range of relevant parameters, geometrical parameters of the HOCM structure were reselected. Dimensions of the initial structure were listed in Table 5, and the parametric influence is numerically discussed based upon equal mass.

5.1. Initial failure modes

For parametric study, different initial failure modes are shown schematically in Fig. 9, with corresponding results presented in Table 6. It can be seen that the failure area is distributed along the diagonal of inclined parallelogram facet, which is attributed to the folding of the 1-direction. When a HOCM structure is subjected to quasi-static out-of-plane compression, the four inclined parallelogram facets tend to expand outward. However, the tendency is constrained by the folding line, contributing to a mixed compression-shear force on the inclined parallelogram facet. Therefore, failure along the diagonal of the facet occurs. Meanwhile, multiple failure modes are produced owing to the hierarchy of structure.

Failure mode A (FA): wrinkling. Under compressive loading, the face sheets can fail via short-wavelength elastic buckling (wrinkling), if the supporting span of inner corrugations for the face sheets is long or the face sheets are thin.

Failure mode B (FB): Plastic yielding (face sheets). When the supporting span of inner corrugations for face sheets and the face sheet thickness are moderate, the face sheets may fail due to plastic yielding.

Failure mode C (FC): Buckling (face sheets). When the slenderness ratio p_1 is large, meaning tall and slender corrugation plates, Euler buckling may occur in the structure.

Failure mode D (FD): Shear buckling. Shear buckling may occur when the face sheets are thin and the supporting force of corrugations is insufficient.

Failure mode E (FE): Euler buckling (corrugated core). This initial failure mode occurs when the corrugations are weak, e.g., the wall thickness ratio p_2 is large.

5.2. Effects of slenderness and wall thickness ratios

Firstly, the influence of slenderness ratio p_1 on peak strength and energy absorption is quantified. The numerically predicted peak strength σ_p and specific peak strength (SPS) $\sigma_p/\bar{\rho}\sigma_{0.2}$ as functions ofp_1, with other parameters fixed at $a = 100$ mm, $l = 76$ mm, $t = t_1 = 0.8$ mm, $s = 1.25l_1$, $\alpha = 60^\circ$, $\beta = 45^\circ$, and $\gamma = 60^\circ$, are plotted in Fig. 10**a**. Corresponding FE simulation results for energy absorption E_v and specific energy absorption (SEA) $E_v/0.5\bar{\rho}\sigma_{0.2}$ are presented in Fig. 10**b**.

The results of Fig. 10 suggest that both the peak stress and energy absorption first increase and then decrease with increasingp_1, and a similar variation trend holds for the SPS and SEA. In addition, both the peak strength and energy absorption (as well as the SPS and SEA) are maximized when$p_1 = 18.5$. This indicates that to achieve enhanced SPS and SEA, the number of corrugations in inclined parallelogram corrugation sandwich plates is preferred to be approximately 12 in this parametric study. For a deeper understanding of the results, the numerically predicted initial failure modes of the samples listed in Table 6 are illustrated in Fig. 10 as well. Three initial failure modes emerge as p_1 is increased. Specifically, a transition from FB to FC occurs where the peak strength and energy absorption decrease. Such transition may decrease the participation of internal corrugations during the deformation process and reduce the number of plastic hinges, since the FC mode introduces an overall buckling of HOCMs' parallelogram plates and leads to less deformation of corrugations.

Secondly, Fig. 11**a** plotted the numerically predicted σ_p and SPS as functions of wall thickness ratiop_2, withp_1 fixed at 9.5, $a = 100$ mm, $l = 76$ mm, $s = 1.25l_1$, $\alpha = 60^\circ$, $\beta = 45^\circ$, and $\gamma = 60^\circ$. Both the σ_p and SPS increase with increasingp_2, but the increasing trend slows rapidly after p_2 exceeds 1. Corresponding plots of E_v and SEA are displayed in Fig. 11**b**. Both increase first and then basically remain unchanged as p_2 is increased, and the turning point occurs at $p_2 = 1$. In all, the overly weak face sheets of inclined parallelogram corrugation sandwich plates are not conducive to the compressive performance of HOCM structures. Additionally, as illustrated in Fig. 11, with the variation ofp_2, three different initial failure modes appear and, when the initial failure mode is changed from FA to other modes, neither the peak strength nor the energy absorption changes significantly.

5.3. Effect of folding angles

In this section, the effect of folding angles α and β on peak strength and energy absorption is investigated, with the remaining parameters constrained as $p_1 = 9.5$, $p_2 = 1$, with $a = 100$ mm, $l = 76$ mm, $s = 1.25l_1$, $t = 0.8$, and $\gamma = 60^\circ$. Fig. 12**a** presents the relationships betweenσ_p, SPS and α, with β fixed as45°. Corresponding results for E_v and SEA are illustrated in Fig. 12**b**. It can be seen that both the peak strength and energy absorption increase with the increase of α, while the SPS and SEA decrease slightly after α exceeds80°. This may be due to the fact that the diagonal pattern of deformation is no longer apparent due to the high value of angle α, hence the region of plastic deformation is reduced. Further, within the studied range of folding angle α, the initial failure mode of FA remains unchanged.

The effect of folding angle β on σ_p and SPS as well as E_v and SEA is shown in Fig. 13**a and b**, respectively, with the other folding angle α fixed at60°. According to Fig. 13**a**, the σ_p increases with increasing β, while the SPS fluctuates when β exceeds45°. Similar variation trend is observed in Fig. 13**b** forE_v, increasing as β is increased. However, the SEA initially increases with increasing β but decreases slightly once β exceeds45°. Similar to the effect of folding angle α, the change in folding angle β does not bring about a transformation in the initial failure mode, which is always FA. For HOCM specimens with small β (e.g., $\beta = 30^\circ$), the stress concentration tends to occur at the folded prongs, making the structure susceptible to fail or deform, which leads to the lower σ_p andE_v.

Table 5
Geometrical parameters of the initial HOCM structure selected for parametric analysis.

Sample	a (mm)	l (mm)	l_1 (mm)	t (mm)	t_1 (mm)	s (mm)	α	β	γ	$\bar{\rho}$
Initial HOCM	100	76	8	0.80	0.80	10	60°	45°	60°	0.049

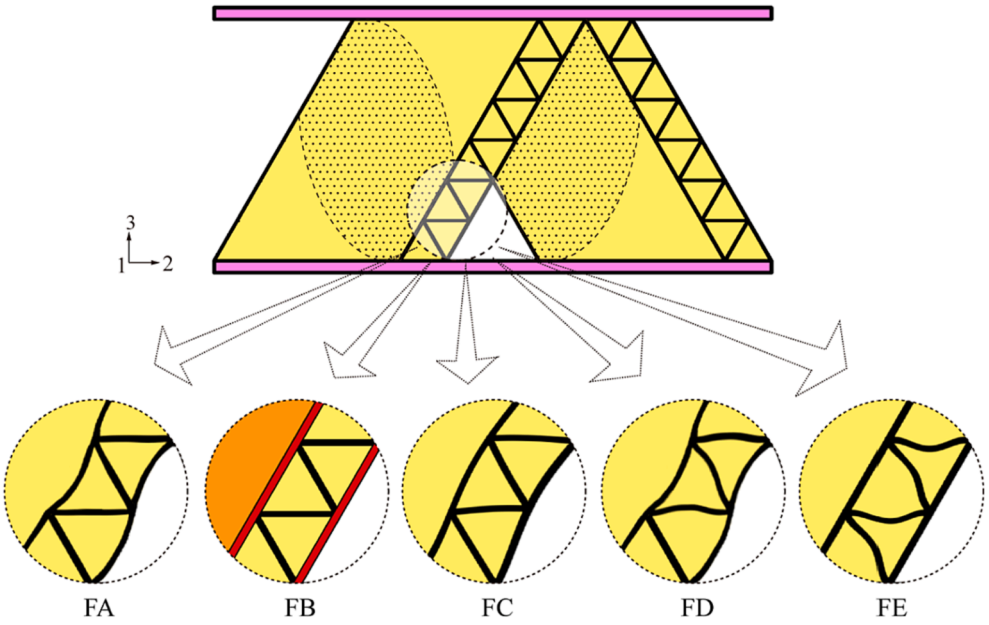

Fig. 9. Initial failure modes of a HOCM structure.

Table 6
Initial failure modes of HOCM specimens selected for parametric study.

No.	p_1	p_2	α (°)	β (°)	Failure mode	Interpretation
1	5	1	60	45	FA	Wrinkling
2	9.5	1	60	45	FA	Wrinkling
3	14	1	60	45	FB	Plastic yielding: face sheets
4	18.5	1	60	45	FB	Plastic yielding: face sheets
5	23	1	60	45	FC	Euler buckling: face sheets
6	9.5	0.5	60	45	FA	Wrinkling
7	9.5	2	60	45	FD	Shear buckling
8	9.5	3	60	45	FD	Shear buckling
9	9.5	4	60	45	FE	Euler buckling: corrugated core
10	9.5	1	50	45	FA	Wrinkling
11	9.5	1	70	45	FA	Wrinkling
12	9.5	1	80	45	FA	Wrinkling
13	9.5	1	85	45	FA	Wrinkling
14	9.5	1	60	30	FA	Wrinkling
15	9.5	1	60	60	FA	Wrinkling
16	9.5	1	60	75	FA	Wrinkling

6. Multi-objective optimal design

A variety of engineering applications (e.g., special vehicles and high-speed trains) demand multifunctional structures that are lightweight and yet possess simultaneously superior stiffness/strength and energy absorption [45,46]. In this section, a multi-objective optimization method combining the fully connected neural network surrogate model (FCNNs) and the non-dominated sorting genetic algorithm II (NSGA-II) is proposed to find optimal HOCM structures that are ultralightweight and possess excellent SPS and SEA with assured stiffness.

6.1. Definition of the optimization problem

According to the analysis in **Section 5**, p_1 plays a more significant role in the compression performance of a HOCM structure thanp_2. Meanwhile, the results also indicate that a larger α is more favorable for enhanced compression performance. However, too large α is not conducive to the manufacturing of the structure. Therefore, in the present study, two geometric parameters (p_1 and β) are identified as the key design variables to generate a design space constrained by $5 \leqslant p_1 \leqslant 35$ and$30° \leqslant \beta \leqslant 80°$, with $p_2 = 1$ and $\alpha = 70°$. Meanwhile, similar to the

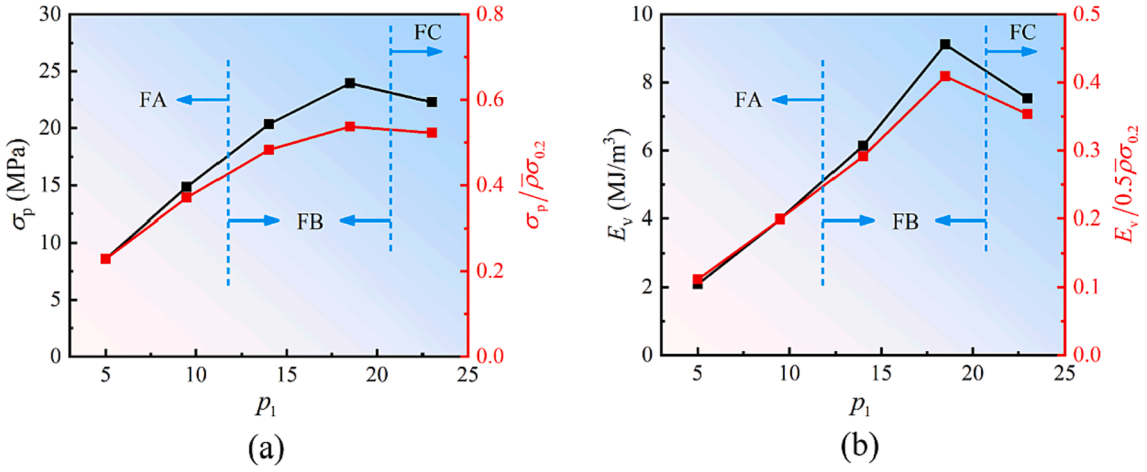

Fig. 10. Effect of slenderness ratio p_1 on (a) peak strength and specific peak strength and (b) energy absorption and specific energy absorption.

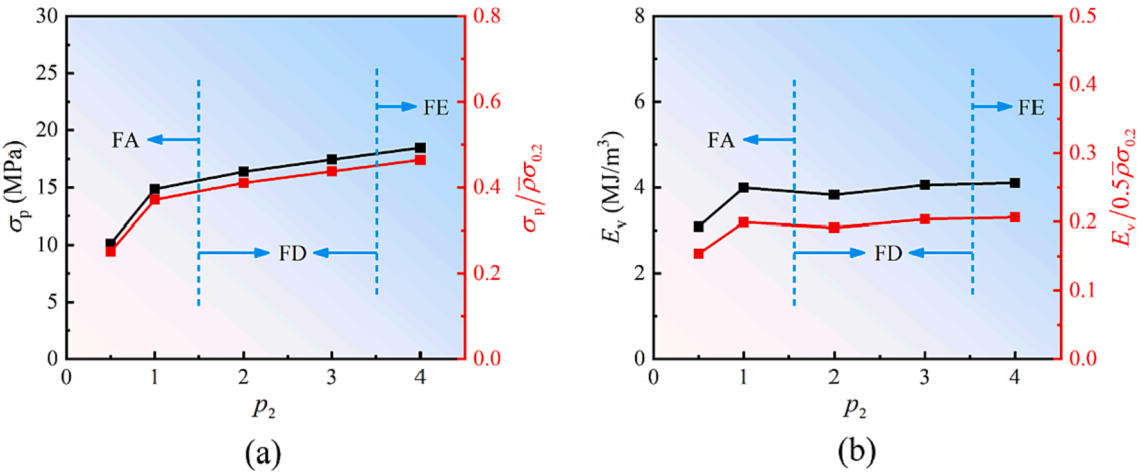

Fig. 11. Effect of wall thickness ratio p_2 on (a) peak strength and specific peak strength and (b) energy absorption and specific energy absorption.

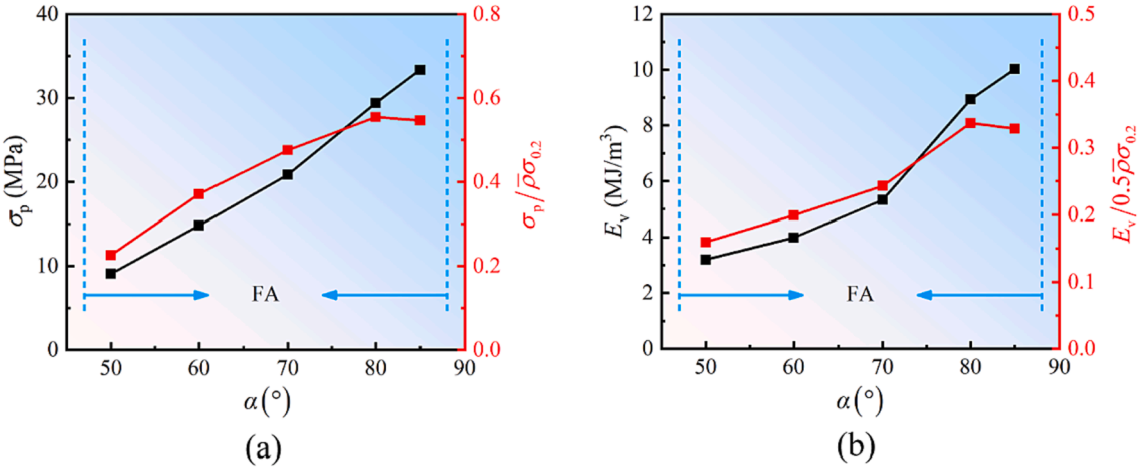

Fig. 12. Effect of folding angle α on (a) peak strength and specific peak strength and (b) energy absorption and specific energy absorption.

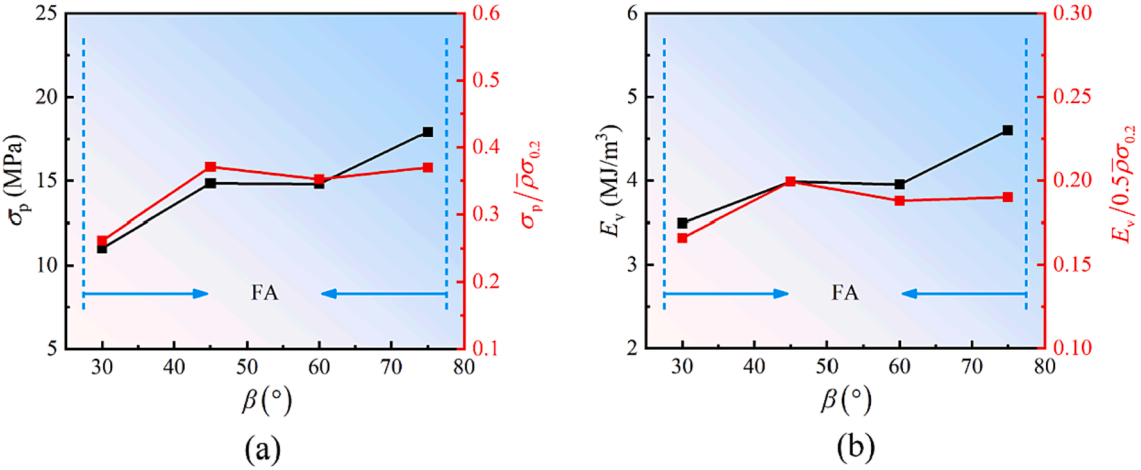

Fig. 13. Effect of folding angle β on (a) peak strength and specific peak strength and (b) energy absorption and specific energy absorption.

foregoing parametric study, the remaining parameters are fixed at a = 100 mm, l = 76 mm, t = 0.8 mm, $s = 1.25l_1$, and γ =60°. Note that, for consistency, the mass of the structure remains unchanged within the design space. Besides, the equivalent compressive modulus is taken as a constraint as well, i.e., the compressive modulus of the optimally designed structure shall not be smaller than that of the initial structure listed in Table 5, which is calculated as 2.24 GPa from Eq. (42). Upon substituting p_1 and p_2 into Eq. (42), the equivalent compressive modulus E^{zzzz} can be expressed as:

$$E^{zzzz} = \frac{(4p_2+2)\sin^3\alpha'\cdot\csc^3\varphi\cdot B^{2'2'2'2'}}{\left[\frac{a}{2t_1}\sin 2\beta + \frac{2l}{t_1}\csc\varphi\cdot\cos\alpha'\cdot\sin\beta + \frac{2l}{t_1 p_1}\sin\gamma\cdot\csc\alpha + (4p_2+2)\csc\alpha\right]} \tag{43}$$

where $B^{2'2'2'2'}$, with p_1, p_2 and $s = 1.25l_1$ substituted into it, is given by:

$$B^{2'2'2'2'} = \frac{E\left[3.5p_2\sin^2\gamma + \left(\frac{t_1}{l}\right)^2 p_1^2(1-\nu^2)(0.25+\cos\gamma)\right]}{1.75(2p_2+1)(1-\nu^2)\sin^2\gamma} \tag{44}$$

Therefore, the equivalent compressive modulus E^{zzzz} can be derived as a function of p_1 and β analytically. The SPS and SEA are thence chosen as the design objectives to evaluate the capacity of the *meta*-sandwich panel for simultaneous load-bearing and energy absorption. However, unlike E^{zzzz}, as both the SPS and SEA exhibit highly nonlinear relationships with the design variables, obtaining an analytical solution for each proves to be difficult. Thus, surrogate modeling based on the technique of machine learning (i.e., FCNNs) is employed for approximate evaluation, with details presented in **Section 6.2**.

In the current study, the optimization problem for the proposed HOCM structures is defined as:

$$\begin{cases} \max \quad \{\mathrm{SPS}(p_1,\beta), \quad \mathrm{SEA}(p_1,\beta)\} \\ \qquad 5\leqslant p_1 \leqslant 35 \\ \qquad 30^\circ \leqslant \beta \leqslant 80^\circ \\ E^{zzzz} \geqslant E_0^{zzzz} \quad (\text{i.e.,} \quad 2.24 \quad \text{GPa}) \end{cases} \tag{45}$$

6.2. Surrogate model

6.2.1. Machine learning method

Generally speaking, the SPS and SEA of a HOCM structure exhibit complicated behaviors, due mainly to its nonlinear structural deformation. Therefore, the ML-based surrogate model, i.e., FCNNs, that was proved efficient for nonlinear problems [25,26,47], is implemented into the present optimization task. To reduce local fluctuations and improve the approximating accuracy, loops are introduced into the machine learning model [48], with the flow chart shown in Fig. 14. As is shown, the FCNNs machine learning model is set up with three layers, with fifty neurons (i.e., temporary random variables, the blue discs in Fig. 14) in each layer, to train the data generated in the design space. To ensure the accuracy of the model, the method introduces four loop iterations. The initial sampling points data set generated in the design space is listed in Table 7, and the other three loops are conducted based on the judgment of approximating accuracy (detailed in **Section 6.2.2**), with their sampling points listed in Table 7 as well.

6.2.2. Accuracy of surrogate model

Following the principle of cross-validation error analysis [49], surrogate accuracy is determined. Specifically, a certain number of validation points are excluded from the sampling point data set, one at a time. The approximation coefficients are recalculated for each of the excluded points, and the actual (FE calculation) and predicted (surrogate model) values are compared. After that, the currently removed point is returned to the sampling point data set, and the next point is removed. Note that, all the points in the data set of one loop are selected to perform cross-validation in this work. Further, the relative error of surrogate models is evaluated using the R-square (R^2) and the Maximum-Absolute-Percentage-Error (MAPE) for global and local accuracy, respectively, as:

$$R^2 = 1 - \frac{\sum_{i=1}^{N}(y_i - \widehat{y}_i)^2}{\sum_{i=1}^{N}(y_i - \overline{y}_i)^2} \tag{46}$$

$$\mathrm{MAPE} = \max\left(\frac{|y_i - \widehat{y}_i|}{y_i}\right) \tag{47}$$

where y_i,$\overline{y}_i$, and $\widehat{y}_i$ are separately the actual (FE calculation) value, the average FE value, and the surrogate model predicted value at these validation points, and N is the number of validation points.

The two quantitative parameters used to evaluate the accuracy of

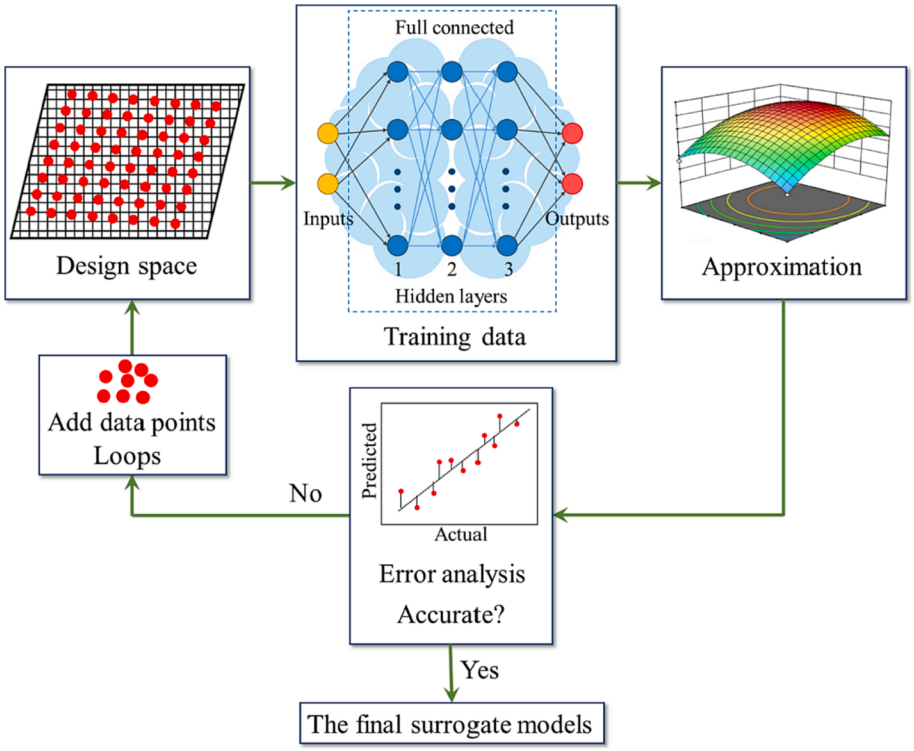

Fig. 14. Flow chart of the FCNNs machine learning method.

Table 7
Sampling points and FE results at these points.

Loops	No.	p_1	β (°)	SPS	SEA	Loops	No.	p_1	β (°)	SPS	SEA
Loop1	1	5	30	0.256	0.144	Loop1	29	27.5	60	0.695	0.481
	2	5	45	0.298	0.138		30	27.5	75	0.666	0.358
	3	5	60	0.304	0.133		31	32	30	0.608	0.485
	4	5	75	0.314	0.108		32	32	45	0.651	0.486
	5	9.5	30	0.433	0.236		33	32	50	0.676	0.486
	6	9.5	45	0.475	0.243		34	32	55	0.671	0.472
	7	9.5	50	0.466	0.242		35	32	60	0.676	0.466
	8	9.5	55	0.488	0.243		36	32	75	0.661	0.385
	9	9.5	60	0.497	0.240	Loop2	37	15.5	65	0.656	0.453
	10	9.5	75	0.514	0.228		38	18.5	55	0.694	0.413
	11	14	30	0.533	0.374		39	20	75	0.690	0.351
	12	14	45	0.596	0.405		40	21.5	55	0.701	0.424
	13	14	50	0.584	0.383		41	23	50	0.686	0.443
	14	14	55	0.594	0.392		42	30.5	30	0.609	0.489
	15	14	60	0.597	0.404		43	35	30	0.596	0.471
	16	14	75	0.601	0.413		44	35	55	0.658	0.443
	17	18.5	30	0.580	0.453	Loop3	45	20	60	0.697	0.395
	18	18.5	45	0.669	0.422		46	21.5	50	0.683	0.429
	19	18.5	60	0.696	0.418		47	21.5	80	0.669	0.295
	20	18.5	75	0.685	0.358		48	26	30	0.608	0.483
	21	23	30	0.626	0.480		49	29	30	0.597	0.484
	22	23	45	0.677	0.442		50	32	80	0.651	0.327
	23	23	60	0.688	0.428		51	33.5	40	0.637	0.478
	24	23	75	0.680	0.344		52	35	40	0.638	0.461
	25	27.5	30	0.604	0.498	Loop4	53	29	65	0.678	0.420
	26	27.5	45	0.652	0.474		54	29	80	0.640	0.300
	27	27.5	50	0.676	0.482		55	30.5	45	0.658	0.444
	28	27.5	55	0.666	0.448		56	33.5	70	0.668	0.396

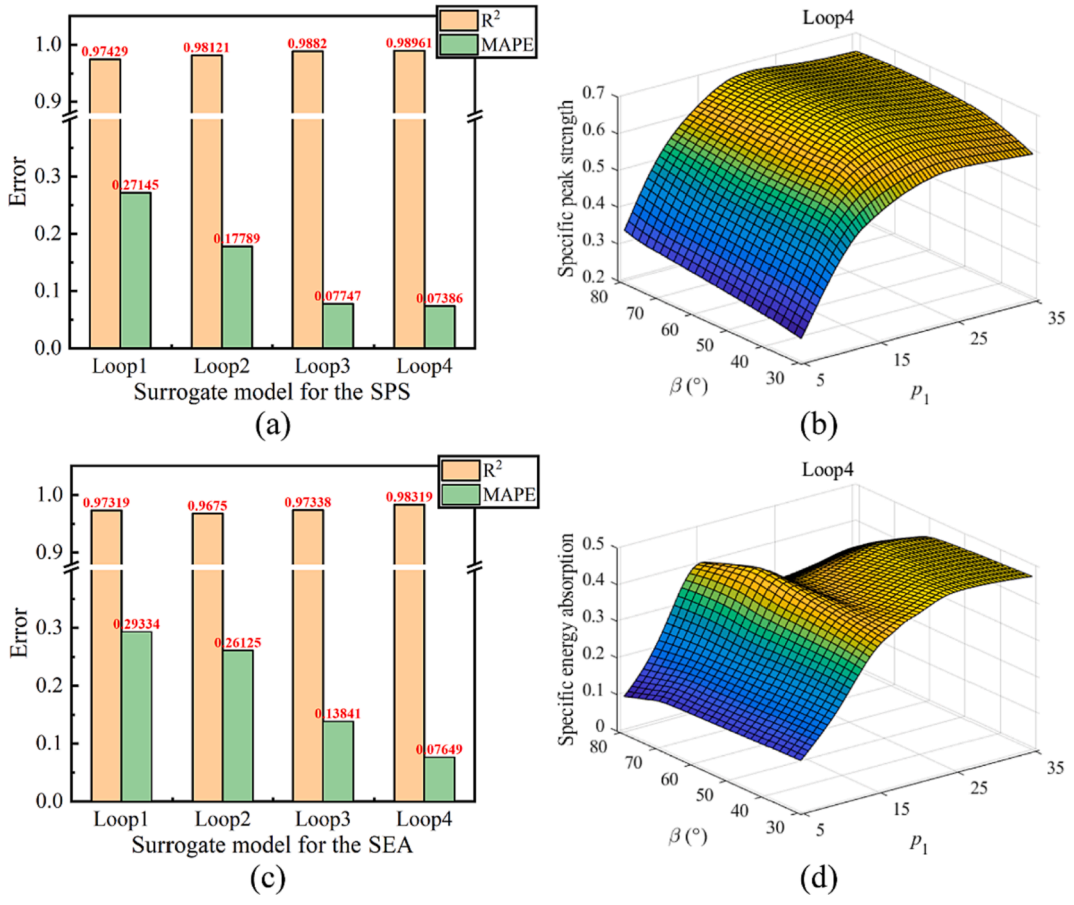

Fig. 15. Error analysis of surrogate models for (a) SPS and (b) SEA and final surrogate models for (c) SPS and (d) SEA.

surrogate models of the four loops are compared in Fig. 15**a and c**. As the loops increase, the MAPE of the surrogate models for both the SPS and SEA decreases significantly, thus indicating obviously improved local accuracy. Meanwhile, the R^2 increases with loops adding up, indicating improved global accuracy as well. After loop4, the R^2 of surrogate models for the SPS and SEA are all greater than 98%, with the MAPE less than 8%, which indicates that the surrogate models exhibit sufficient accuracy. The surrogate modeling task based on machine learning is thus completed. Fig. 15**b and c** present the results of surrogate models for the SPS and SEA, respectively. It can be seen that the function between the SEA and design variables is more nonlinear than that of the SPS.

Next, to further demonstrate the advantages of machine learning, the nonlinear multiple regression method based on the polynomial fitting algorithm, commonly used to predict the compressive performances of cellular structures/tubes [35,50,51], is employed as another strategy to obtain surrogate models for both the SPS and SEA. For brevity, the detailed functions are presented in **Appendix A**. As shown in Fig. 16**a and b**, the surrogate model obtained by the nonlinear multiple regression fitting method for the SPS is similar to the machine learning result (loop4), while the nonlinear multiple regression fitting result for the SEA is quite different from that predicted via machine learning. The strongly nonlinear behavior can not be characterized accurately by such a traditional method. As presented in Fig. 16**c and d**, the R^2 of the surrogate model obtained by nonlinear multiple regression fitting of the SEA is only 90.569% while the MAPE is more than 50%, which is much worse than the machine learning method, though the R^2 and MAPE of the SPS of both methods are similar. Note that, the sampling points for performing nonlinear multiple regression include all data from the 4 loops in the machine learning method, which are encrypted at the stronger nonlinearity. In other words, even though the traditional method inherits an excellent sample set, its surrogate model for the strongly nonlinear condition is still not accurate enough compared to the present method based on machine learning.

6.3. Optimization algorithm

To determine the optimal configuration of the proposed HOCM structure for superior SPS and SEA, the NSGA-II multi-objective optimization algorithm [52] is employed. For non-dominant sorting, the NSGA-II algorithm adopts an elite retention technique and a no-parameter niche operation, which solves problems of high computational complexity, poor algorithm execution speed, and the need to determine the shared radius in conventional nondominant sorting genetic algorithms [52]. It is thus widely applied in the optimizations to approach the true Pareto front. For the present optimal task, the key parameters of this algorithm, i.e., the population size, number of generations, crossover probability, crossover distribution index and mutation distribution index, are set as 100, 200, 0.9, 20 and 40, respectively.

6.4. Optimization results

For a HOCM structure, the present optimization aims to achieve optimal performance of its SPS and SEA, subjected to the constraints listed in **Section 6.1**. Conflict between the two design objectives usually leads to a Pareto set where each point represents an optimal design in different situations. The Pareto set obtained for the present optimization problem is presented in Fig. 17**a**. To compare with the initial structure design in **Section 5**, the Pareto set is processed and redrawn in the form of enhancement ratio as shown in Fig. 17**b**. It can be seen that the two objectives (SPS and SEA) of the optimal design results exhibit significant enhancement of 64.73–86.83% and 114.04–144.95%, respectively. The distribution of Pareto set in the design space is presented in Fig. 17**c** for the SPS and in Fig. 17**d** for the SEA, respectively. It can be found that the design variables (p_1 and β) at these points vary in the range of $21.86 \leqslant p_1 \leqslant 27.56$ and $30^\circ \leqslant \beta \leqslant 54.52^\circ$, respectively. These results suggest that the number of corrugations in inclined parallelogram corrugated sandwich plates should not be too few or too many, preferably 14–18, and the folding angle β should not be too large.

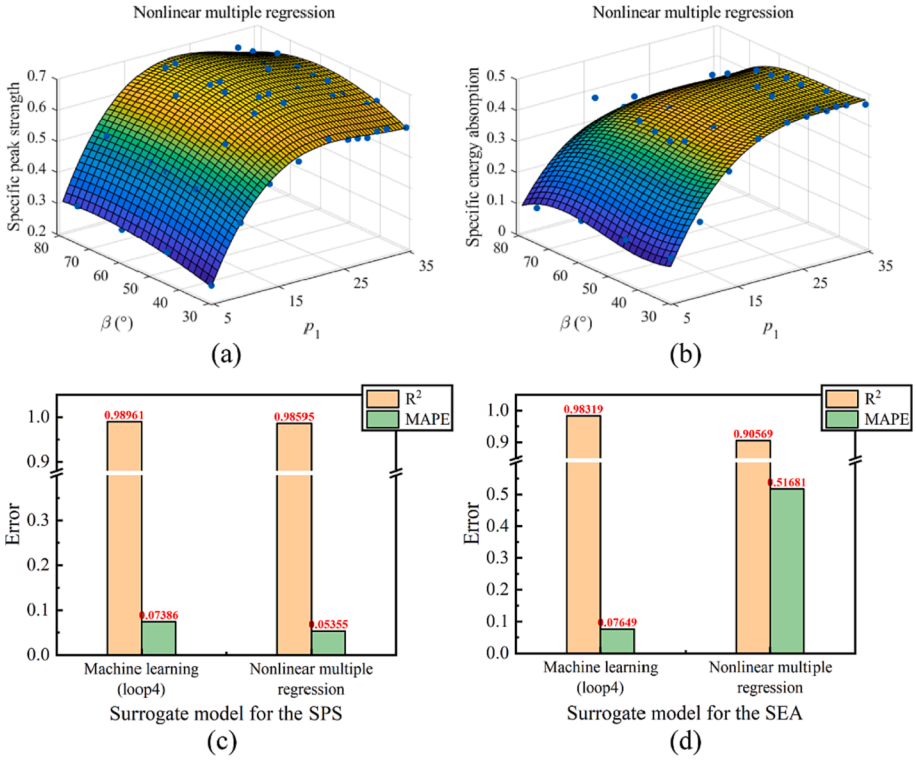

Fig. 16. Surrogate models predicted through nonlinear multiple regression with a full cubic polynomial fit of (a) specific peak strength and (b) specific energy absorption; error analysis of surrogate models predicted by machine learning and nonlinear multiple regression for (c) specific peak strength and (d) specific energy absorption.

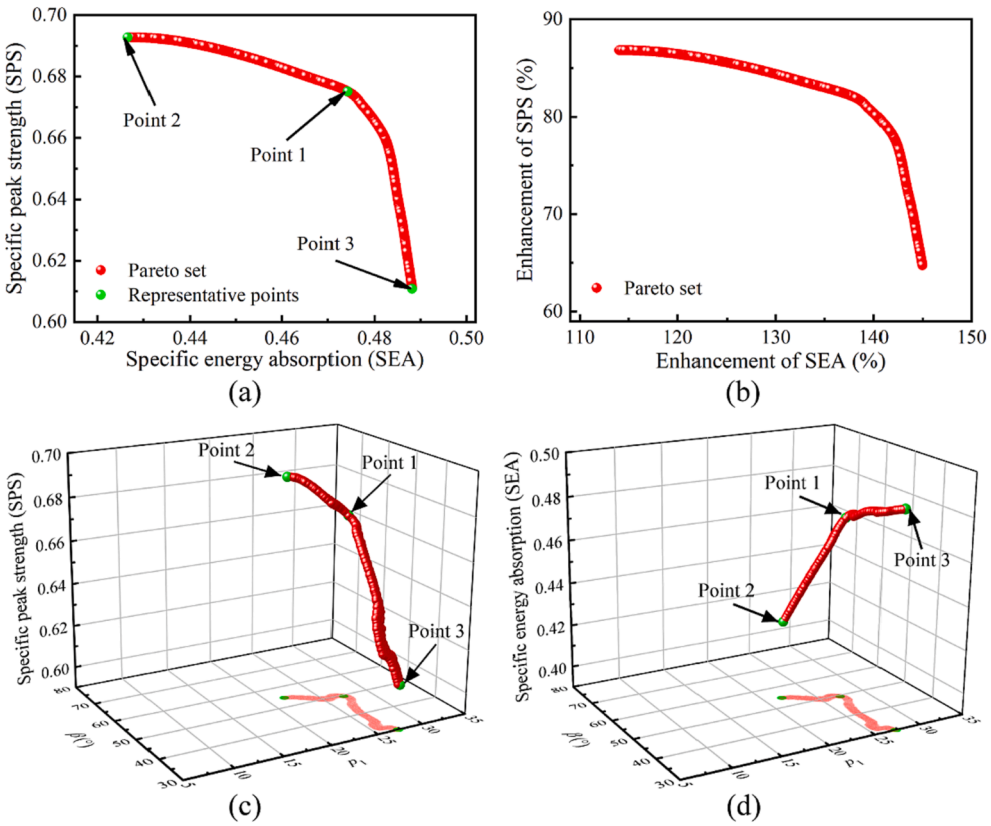

Fig. 17. Optimal design results: (a) Pareto set and (b) enhancement ratio of Pareto set. Distribution of Pareto set in design space: (a) specific peak strength and (b) specific energy absorption.

Finally, to verify the accuracy of present optimization results, the HOCM structures corresponding to three representative points in the Pareto set (marked in Fig. 17**a**) are selected for FE simulations. As shown in Table 8, the error between the numerical results and optimization solutions are all less than 2%, thus confirming the reliability of the present optimization approach.

7. Conclusions

With focus placed upon revealing the parametric sensitivity on the compressive performance of a hierarchical origami-corrugation *meta*-sandwich (HOCM) structure, an analytical approach to predict its macro-equivalent compressive modulus has been developed, while a multi-objective optimization strategy associated with a surrogate model based on a fully connected neural network (FCNN) algorithm has been employed to explore further its compressive strength and energy absorption capacity. Main findings are summarized as follows:

(i) The proposed two-level homogenization approach can efficiently predict the macro-equivalent compressive modulus of HOCM structures.

(ii) Comparison between experimental results and finite element simulations reveals that the selected representative volume element (RVE) can well mimic the compressive performance of HOCM structures.

(iii) Five initial failure modes in the hierarchical architecture of HOCM structure are captured via parametric study. Its specific peak strength (SPS) and specific energy absorption (SEA) exhibit different sensitivities to key geometric parameters. The effect of slenderness ratio on compressive performance is found to be significant.

(iv) Under the principles of cross-validation, the surrogate model based on the FCNN algorithm provides highly efficient accuracy for both the SPS and SEA. Compared to the traditional approximation method, the machine learning method adopted in the present study exhibits high accuracy for strongly nonlinear problems, especially when the SEA needs to be predicted.

(v) For multi-objective optimizations of the HOCM structure, the Pareto set provides significant enhancement in both the SPS and SEA: up to 87% for the former, and 150% for the latter. Results obtained with the optimization strategy are validated against finite element simulation results.

Table 8
Comparison between FE calculation results and optimized solutions.

Specimen	p_1	β (°)	Compressive modulus (GPa)	Objectives	ML surrogate model	FE model	Error (%)
Point 1	27.15	49.44	3.8566	SPS	0.6752	0.6799	−0.69
				SEA	0.4742	0.4823	−1.68
Point 2	21.86	54.42	3.8571	SPS	0.6928	0.6883	0.65
				SEA	0.4266	0.4292	−0.61
Point 3	27.24	30	4.0807	SPS	0.6108	0.6104	0.07
				SEA	0.4882	0.4881	0.02

CRediT authorship contribution statement

Zengshen Yue: Conceptualization, Investigation, Formal analysis, Methodology, Visualization, Writing – original draft. **Bin Han:** Conceptualization, Funding acquisition, Supervision, Writing - review & editing. **Zeyu Wang:** Software, Data curation. **Mao Yang:** Methodology. **Qi Zhang:** Resources, Funding acquisition. **Tian Jian Lu:** Supervision, Funding acquisition, Writing – review & editing.

Declaration of Competing Interest

The authors declare that they have no known competing financial interests or personal relationships that could have appeared to influence the work reported in this paper.

Data availability

The authors do not have permission to share data.

Acknowledgments

This work was supported by the National Natural Science Foundation of China (No. 11802221, 51875441, 11972185, and 12032010), the Fundamental Research Funds for the Central Universities (No. xtr012019004 and zrzd2017027).

Appendix A

To obtain surrogate models of specific peak strength (SPS) and specific energy absorption (SEA) for HOCM structures by using the method of nonlinear multiple regression, the full cubic polynomial functions are employed. Specifically, as given below, formula (A. 1) is the function for SPS of HOCM structures, while formula (A. 2) is the function for SEA of HOCM structures:

$$\begin{aligned}\mathrm{SPS} = {} & -0.1061 + 0.0649p_1 + 0.0017\beta - 0.0025p_1^2 + 2.7940\times10^{-4}p_1\beta \\ & +1.7031\times10^{-5}\beta^2 + 2.8644\times10^{-5}p_1^3 - 2.4615\times10^{-6}p_1^2\beta \\ & -1.8291\times10^{-6}p_1\beta^2 - 2.8936\times10^{-7}\beta^3\end{aligned} \tag{A. 1}$$

$$\begin{aligned}\mathrm{SEA} = {} & 0.2985 + 0.0617p_1 - 0.0297\beta - 0.0021p_1^2 + 7.8456\times10^{-5}p_1\beta \\ & +6.1239\times10^{-4}\beta^2 + 2.1960\times10^{-5}p_1^3 + 3.1116\times10^{-6}p_1^2\beta \\ & -2.8163\times10^{-6}p_1\beta^2 - 3.8243\times10^{-6}\beta^3\end{aligned} \tag{A. 2}$$

References

[1] Da Silva A, Kyriakides S. Compressive response and failure of balsa wood. Int J Solids Struct 2007;44:8685–717. https://doi.org/10.1016/j.ijsolstr.2007.07.003.
[2] Van Liedekerke P, Ghysels P, Tijskens E, Samaey G, Smeedts B, Roose D, et al. A particle-based model to simulate the micromechanics of single-plant parenchyma cells and aggregates. Phys Biol 2010;7(2):026006.
[3] Ryan TM, Shaw CN. Trabecular bone microstructure scales allometrically in the primate humerus and femur. Proc Roy Soc B: Biol Sci 2013;280:20130172. https://doi.org/10.1098/rspb.2013.0172.
[4] Seki Y, Bodde SG, Meyers MA. Toucan and hornbill beaks: a comparative study. Acta Biomater 2010;6:331–43. https://doi.org/10.1016/j.actbio.2009.08.026.
[5] Zheng X, Lee H, Weisgraber TH, Shusteff M, DeOtte J, Duoss EB, et al. Ultralight, ultrastiff mechanical metamaterials. Science 2014;344(6190):1373–7.
[6] Han B, Qin K, Yu B, Wang B, Zhang Q, Lu TJ. Honeycomb-corrugation hybrid as a novel sandwich core for significantly enhanced compressive performance. Mater Des 2016;93:271–82. https://doi.org/10.1016/j.matdes.2015.12.158.
[7] Frenzel T, Kadic M, Wegener M. Three-dimensional mechanical metamaterials with a twist. Science 2017;358:1072–4. https://doi.org/10.1126/science.aao4640.
[8] Li T, Chen Y, Hu X, Li Y, Wang L. Exploiting negative Poisson's ratio to design 3D-printed composites with enhanced mechanical properties. Mater Des 2018;142:247–58. https://doi.org/10.1016/j.matdes.2018.01.034.
[9] Hamzehei R, Kadkhodapour J, Anaraki AP, Rezaei S, Dariushi S, Rezadoust AM. Octagonal auxetic metamaterials with hyperelastic properties for large compressive deformation. Int J Mech Sci 2018;145:96–105. https://doi.org/10.1016/j.ijmecsci.2018.06.040.
[10] Zhang W, Zhao S, Scarpa F, Wang J, Sun R. In-plane mechanical behavior of novel auxetic hybrid metamaterials. Thin-Walled Struct 2021;159:107191. https://doi.org/10.1016/j.tws.2020.107191.
[11] Chen Y, Jia Z, Wang L. Hierarchical honeycomb lattice metamaterials with improved thermal resistance and mechanical properties. Compos Struct 2016;152:395–402. https://doi.org/10.1016/j.compstruct.2016.05.048.
[12] Mahadevan L, Rica S. Self-organized origami. Science 2005;307:1740. https://doi.org/10.1126/science.1105169.
[13] Zhou X, Wang H, You Z. Mechanical properties of Miura-based folded cores under quasi-static loads. Thin-Walled Struct 2014;82:296–310. https://doi.org/10.1016/j.tws.2014.05.001.
[14] Baer E, Hiltner A, Keith H. Hierarchical structure in polymeric materials. Science 1987;235:1015–22. https://doi.org/10.1126/science.3823866.
[15] Côté F, Russell BP, Deshpande VS, Fleck NA. The through-thickness compressive strength of a composite sandwich panel with a hierarchical square honeycomb sandwich core. J Appl Mech 2009;76:061004. https://doi.org/10.1115/1.3086436.
[16] Feng LJ, Yang ZT, Yu GC, Chen XJ, Wu LZ. Compressive and shear properties of carbon fiber composite square honeycombs with optimized high-modulus hierarchical phases. Compos Struct 2018;201:845–56. https://doi.org/10.1016/j.compstruct.2018.06.080.
[17] Yin S, Wu L, Nutt S. Stretch–bend-hybrid hierarchical composite pyramidal lattice cores. Compos Struct 2013;98:153–9. https://doi.org/10.1016/j.compstruct.2012.11.004.
[18] Kooistra GW, Deshpande V, Wadley HNG. Hierarchical corrugated core sandwich panel concepts. J Appl Mech 2007;74:259–68. https://doi.org/10.1115/1.2198243.
[19] Sun G, Jiang H, Fang J, Li G, Li Q. Crashworthiness of vertex based hierarchical honeycombs in out-of-plane impact. Mater Des 2016;110:705–19. https://doi.org/10.1016/j.matdes.2016.08.032.
[20] Qiao J, Chen C. In-plane crushing of a hierarchical honeycomb. Int J Solids Struct 2016;85–86:57–66. https://doi.org/10.1016/j.ijsolstr.2016.02.003.
[21] Dong L. Mechanical response of Ti–6Al–4V hierarchical architected metamaterials. Acta Mater 2019;175:90–106. https://doi.org/10.1016/j.actamat.2019.06.004.
[22] Han B, Yue Z, Wu H, Zhang Q, Lu TJ. Superior compressive performance of hierarchical origami-corrugation metallic sandwich structures based on selective laser melting. Compos Struct 2022;300:116181.
[23] Shakeri M, Mirzaeifar R, Salehghaffari S. New insights into the collapsing of cylindrical thin-walled tubes under axial impact load. Proc Inst Mech Eng, C: J Mech Eng Sci 2007;221:869–85. https://doi.org/10.1243/09544062JMES562.
[24] Liu X, Athanasiou CE, Padture NP, Sheldon BW, Gao H. A machine learning approach to fracture mechanics problems. Acta Mater 2020;190:105–12. https://doi.org/10.1016/j.actamat.2020.03.016.
[25] Li X, Roth CC, Mohr D. Machine-learning based temperature- and rate-dependent plasticity model: application to analysis of fracture experiments on DP steel. Int J Plast 2019;118:320–44. https://doi.org/10.1016/j.ijplas.2019.02.012.
[26] Jordan B, Gorji MB, Mohr D. Neural network model describing the temperature- and rate-dependent stress-strain response of polypropylene. Int J Plast 2020;135:102811. https://doi.org/10.1016/j.ijplas.2020.102811.
[27] Wang GG, Shan S. Review of metamodeling techniques in support of engineering design optimization. J Mech Des 2006;129:370–80. https://doi.org/10.1115/1.2429697.
[28] Fang J, Sun G, Qiu N, Kim NH, Li Q. On design optimization for structural crashworthiness and its state of the art. Struct Multidisc Optim 2017;55:1091–119. https://doi.org/10.1007/s00158-016-1579-y.
[29] Rahmatnezhad K, Zarastvand MR, Talebitooti R. Mechanism study and power transmission feature of acoustically stimulated and thermally loaded composite shell structures with double curvature. Compos Struct 2021;276:114557. https://doi.org/10.1016/j.compstruct.2021.114557.

[30] Wang W, Yang X, Han B, Zhang Q, Wang X, Lu T. Analytical design of effective thermal conductivity for fluid-saturated prismatic cellular metal honeycombs. Theor Appl Mech Lett 2016;6:69–75. https://doi.org/10.1016/j.taml.2016.01.003.
[31] Han B, Zhang ZJ, Zhang QC, Zhang Q, Lu TJ, Lu BH. Recent advances in hybrid lattice-cored sandwiches for enhanced multifunctional performance. Extreme Mech Lett 2017;10:58–69. https://doi.org/10.1016/j.eml.2016.11.009.
[32] Acar E, Guler MA, Gerçeker B, Cerit ME, Bayram B. Multi-objective crashworthiness optimization of tapered thin-walled tubes with axisymmetric indentations. Thin-Walled Struct 2011;49:94–105. https://doi.org/10.1016/j.tws.2010.08.010.
[33] Yin H, Xiao Y, Wen G, Qing Q, Wu X. Crushing analysis and multi-objective optimization design for bionic thin-walled structure. Mater Des 2015;87:825–34. https://doi.org/10.1016/j.matdes.2015.08.095.
[34] Bigdeli A, Nouri MD. A crushing analysis and multi-objective optimization of thin-walled five-cell structures. Thin-Walled Struct 2019;137:1–18. https://doi.org/10.1016/j.tws.2018.12.033.
[35] Yang M, Han B, Su P, Li F, Zhao Z, Zhang Q, et al. Oblique crushing of truncated conical sandwich shell with corrugated core. Mech Adv Mater Struct 2021;28(23):2458–71.
[36] Asanjarani A, Dibajian SH, Mahdian A. Multi-objective crashworthiness optimization of tapered thin-walled square tubes with indentations. Thin-Walled Struct 2017;116:26–36. https://doi.org/10.1016/j.tws.2017.03.015.
[37] Wang E, Li Q, Sun G. Computational analysis and optimization of sandwich panels with homogeneous and graded foam cores for blast resistance. Thin-Walled Structures 2020;147:106494. https://doi.org/10.1016/j.tws.2019.106494.
[38] Wang X, Li X, Yue ZS, Yu RP, Zhang QC, Du SF, et al. Optimal design of metallic corrugated sandwich panels with polyurea-metal laminate face sheets for simultaneous vibration attenuation and structural stiffness. Compos Struct 2021;256:112994.
[39] Talebitooti R, Zarastvand M, Darvishgohari H. Multi-objective optimization approach on diffuse sound transmission through poroelastic composite sandwich structure. J Sandwich Struct Mater 2021;23:1221–52. https://doi.org/10.1177/1099636219854748.
[40] Talebitooti R, Gohari HD, Zarastvand MR. Multi objective optimization of sound transmission across laminated composite cylindrical shell lined with porous core investigating Non-dominated Sorting Genetic Algorithm. Aerosp Sci Technol 2017;69:269–80. https://doi.org/10.1016/j.ast.2017.06.008.
[41] Samanta A, Mukhopadhyay M. Finite element static and dynamic analyses of folded plates. Eng Struct 1999;21:277–87. https://doi.org/10.1016/S0141-0296(97)90172-3.
[42] Han B, Qin KK, Yu B, Zhang QC, Chen CQ, Lu TJ. Design optimization of foam-reinforced corrugated sandwich beams. Compos Struct 2015;130:51–62. https://doi.org/10.1016/j.compstruct.2015.04.022.
[43] Raghavan N, Dehoff R, Pannala S, Simunovic S, Kirka M, Turner J, et al. Numerical modeling of heat-transfer and the influence of process parameters on tailoring the grain morphology of IN718 in electron beam additive manufacturing. Acta Mater 2016;112:303–14.
[44] Sangid MD, Book TA, Naragani D, Rotella J, Ravi P, Finch A, et al. Role of heat treatment and build orientation in the microstructure sensitive deformation characteristics of IN718 produced via SLM additive manufacturing. Addit Manuf 2018;22:479–96.
[45] Zhang DuJiang, Zhao ZhenYu, Du ShaoFeng, Chen WeiJie, Yang F, Ni ChangYe, et al. Dynamic response of ultralight all-metallic sandwich panel with 3D tube cellular core to shallow-buried explosives. Sci China Technol Sci 2021;64(7):1371–88.
[46] Zhang M, Yu Q, Liu Z, Zhang J, Tan G, Jiao D, et al. 3D printed Mg-NiTi interpenetrating-phase composites with high strength, damping capacity, and energy absorption efficiency. Sci Adv 2020;6(19). https://doi.org/10.1126/sciadv.aba5581.
[47] Marzbanrad J, Ebrahimi MR. Multi-objective optimization of aluminum hollow tubes for vehicle crash energy absorption using a genetic algorithm and neural networks. Thin-Walled Struct 2011;49:1605–15. https://doi.org/10.1016/j.tws.2011.08.009.
[48] Xue D, Balachandran PV, Hogden J, Theiler J, Xue D, Lookman T. Accelerated search for materials with targeted properties by adaptive design. Nat Commun 2016;7:1–9. https://doi.org/10.1038/ncomms11241.
[49] Browne MW. Cross-validation methods. J Math Psychol 2000;44:108–32. https://doi.org/10.1006/jmps.1999.1279.
[50] Yang M, Han B, Su P-B, Wei Z-H, Zhang Qi, Zhang Q-C, et al. Axial crushing of ultralight all-metallic truncated conical sandwich shells with corrugated cores. Thin-Walled Struct 2019;140:318–30.
[51] Yang M, Han B, Su P, Zhang Q, Zhang Q, Zhao Z, et al. Crashworthiness of hierarchical truncated conical shells with corrugated cores. Int J Mech Sci 2021;193:106171. https://doi.org/10.1016/j.ijmecsci.2020.106171.
[52] Deb K, Pratap A, Agarwal S, Meyarivan T. A fast and elitist multiobjective genetic algorithm: NSGA-II. IEEE Trans Evol Comput 2002;6:182–97. https://doi.org/10.1109/4235.996017.